Journal of Catalysis 340 (2016) 302–320

Contents lists available at ScienceDirect

Journal of Catalysis

journal homepage: www.elsevier.com/locate/jcat

Condensation and esterification reactions of alkanals, alkanones, and alkanols on TiO_2: Elementary steps, site requirements, and synergistic effects of bifunctional strategies

Shuai Wang, Konstantinos Goulas [1], Enrique Iglesia *

Department of Chemical and Biomolecular Engineering, University of California at Berkeley, Berkeley, CA 94720, USA

ARTICLE INFO

Article history:
Received 14 April 2016
Revised 27 May 2016
Accepted 29 May 2016

Keywords:
TiO_2
Aldol condensation
Esterification
Oxygenate catalysis
Enolates
Bifunctional stabilization
Density functional theory
Site titrations

ABSTRACT

Rates and selectivity of TiO_2-catalyzed condensation of C_3 oxygenates (propanal, acetone) are limited by ubiquitous effects of side reactions, deactivation, and thermodynamic bottlenecks. H_2 together with a Cu function, present as physical mixtures with TiO_2, circumvents such hurdles by scavenging unsaturated intermediates. They also render alkanols and alkanals/alkanones equivalent as reactants through rapid interconversion, while allowing esterification turnovers by dehydrogenating unstable hemiacetals. Oxygenates form molecules with new C—C and C—O bonds and fewer O-atoms at nearly complete conversions with stable rates and selectivities. Kinetic, isotopic, and theoretical methods showed that rates are limited by α-C—H cleavage from carbonyl reactants to form enolate intermediates, which undergo C—C coupling with another carbonyl species to form α,β-unsaturated oxygenates or with alkanols to form hemiacetals with new C—O bonds, via an intervening H-shift that forms alkoxide–alkanal pairs. Titrations with 2,6-di-tert-butylpyridine, pyridine, CO_2, and propanoic acid during catalysis showed that Lewis acid–base site pairs of moderate strength mediate enolate formation steps via concerted interactions with the α-H atom and the enolate moiety at transition states. The resulting site-counts allow rigorous comparisons between theory and experiments and among catalysts on the basis of turnover rates and activation free energies. Theoretical treatments give barriers, kinetic isotope effects, and esterification/-condensation ratios in excellent agreement with experiments and confirm the strong effects of reactant substituents at the α-C-atom and of surface structure on reactivity. Surfaces with Ti—O—Ti sites exhibiting intermediate acid–base strength and Ti—O distances, prevalent on anatase but not rutile TiO_2, are required for facile α-C—H activation in reactants and reprotonation of the adsorbed intermediates that mediate condensation and esterification turnovers.

1. Introduction

Aldol condensations of carbonyl compounds form conjugated α,β-unsaturated oxygenates with longer chains and lower O-content than in the reactant molecules [1–3]. Such products can be used as chemical intermediates or converted via H_2-mediated deoxygenation reactions to alkanes and alkenes, and are useful as fuels and as chemical intermediates within existing market infrastructures [4–11]. Aldol condensations represent a potential enabling strategy for upgrading biomass-derived feedstocks, which contain fewer C-atoms and more O-atoms than their desired conversion products [2,3].

Metal oxides (e.g., MgO [12,13], $MgO—Al_2O_3$ [14–17], ZrO_2 [6,18], $CeO_2—ZrO_2$ [19,20], and TiO_2 [21–23]) catalyze aldol condensation reactions. On these oxide catalysts, reactions are limited by thermodynamics [15], leading to low equilibrium concentrations of α,β-unsaturated carbonyl compounds; these compounds tend to undergo subsequent condensation and cyclization reactions that form unreactive residues and block active sites [22,23]. With added H_2, metal particles supported on the oxide catalysts (e.g., Pt [17], Pd [17,24], and Cu [25]) hydrogenate these unsaturated primary products to more stable saturated products, thus removing thermodynamic bottlenecks and inhibiting deactivation; these effects of the hydrogenation function, however, have not been assessed quantitatively or systematically using physical mixtures that allow the independent optimization of the condensation and hydrogenation functions.

Aldol condensations on oxides involve enolate formation via C—H activation at the α-position to the carbonyl group (C=O) in

---

* Corresponding author.
E-mail address: iglesia@berkeley.edu (E. Iglesia).

[1] Current address: Catalysis Center for Energy Innovation, University of Delaware, Newark, DE 19716, USA.

http://dx.doi.org/10.1016/j.jcat.2016.05.026

alkanals and alkanones, subsequent nucleophilic attack by another carbonyl compound to form a new C—C bond in the aldol formed, and dehydration of the aldol intermediate and desorption as a gaseous conjugated enal or enone [26], in steps resembling those in their homogeneous reaction analogs [25]. The inhibition of acetone condensation rates on MgO by added pyridine and acetic acid indicates that both acid and basic sites may be involved [12]; infrared spectra have shown that basic O-atoms abstract the α-H-atoms in carbonyl compounds, while acid centers can stabilize enolates via interactions with the O-atoms of the enolates [18,27]. The kinetic relevance of these steps remains unconfirmed by kinetic, isotopic, or spectroscopic methods and based solely on theoretical treatments on ZrO_2 and CeO_2 surfaces [28].

The ubiquitous thermodynamic and deactivation hurdles have prevented detailed kinetic and isotopic analyses of the elementary steps that mediate these reactions. These matters also preclude the identification and counting of the active sites during catalysis, essential to compare catalysts based on turnover rates, and an accurate measurement of the activation free energies, which are required for theoretical benchmarking of proposed mechanisms and turnover rates.

In this study, we use physical mixtures of Cu/SiO_2 with TiO_2(P25) (a mixture of anatase (TiO_2(a)) and rutile (TiO_2(r)) crystal phases, anatase/rutile ratio of 3), pure TiO_2(a), or TiO_2(r) as bifunctional catalysts for the aldol condensation of C_3 oxygenates (propanal, 1-propanol, acetone, and 2-propanol). The presence of a Cu function and of H_2 leads to higher turnover rates and much slower deactivation by overcoming thermodynamic hurdles and scavenging unsaturated precursors to unreactive residues. The Cu function also enables the equilibration of alkanals and alkanones with their respective alkanols, thus allowing their interchangeable use as reactants. The unprecedented stability conferred by the Cu function allows detailed kinetic measurements, rigorous comparisons of areal rates on TiO_2(a) and TiO_2(r), site titrations during catalysis (with CO_2, 2,6-di-tert-butylpyridine (DTBP), pyridine, and propanoic acid), and mechanistic studies of the elementary steps and active site structures that mediate these reactions.

Acid–base site pairs of intermediate strength and site distance prevalent on TiO_2(a), probed by titrations during catalysis, account for its higher reactivity and stability than TiO_2(r), as evidenced from the reversible rate inhibition by pyridine and propanoic acid, but the absence of inhibition by selective titrants of only basic (CO_2) or only Brønsted acid (DTBP) sites. The number of acid–base site pairs was measured by titration with propanoic acid during condensation reactions, thus allowing the first rigorous measurements of intrinsic turnover rates and activation free energies. Conversion rates were proportional to reactant pressures for all carbonyl species and showed normal kinetic isotope effects, consistent with the kinetic relevance of α-C—H cleavage to form enolate intermediates; these species then react with a carbonyl compound to form condensation products or (in the case of alkanals) with a terminal alkanol to form esters. These conclusions were confirmed by the observed effects of alkanol/alkanal ratios on the ratio of esterification/condensation rates.

Density function theory (DFT) treatments of plausible condensation and esterification elementary steps on TiO_2(a) cluster models are consistent with these conclusions and give excellent agreement with measured turnover rates and isotope effects for acetone and propanal reactants and with the observed effects of substituents on enolate formation rates and on condensation/esterification rate ratios. Similar treatments on TiO_2(r) cluster models show that condensation rates are limited by reprotonation and desorption of the dimer species formed in carbonyl-enolate coupling steps; such markedly different reactivities in rutile and anatase phases of TiO_2 reflect the spatial separation and strong acid–base strength of exposed Ti—O site pairs on TiO_2(r) surfaces. These mechanistic conclusions and practical bifunctional strategies appear to be general for C_2–C_5 alkanals and alkanones and their respective alkanols on TiO_2 surfaces and to condensation and esterification reactions catalyzed by monoclinic and tetragonal ZrO_2 [29], thus providing general predictive guidance for the complex reaction networks involved in the upgrading of their biomass-derived mixtures.

2. Methods

2.1. Catalyst synthesis and characterization

Cu/SiO_2 (~20 wt.% Cu) was prepared using a homogeneous de position–precipitation method [30], and used as a co-catalyst together with H_2 to improve aldol condensation rates, selectivity, and stability. Colloidal silica (30 wt.%, 21.8 g, LUDOX SM-30), Cu $(NO_3)_2 \cdot 2.5H_2O$ (99.99%, 6.0 g, Sigma–Aldrich) and urea (99%, 4.7 g, Aldrich) were dissolved in deionized water (17.9 MΩ resistivity, 100 cm^3) and the suspension pH was adjusted to 2–3 using a HNO_3 solution (0.5 mmol cm^{-3}; Sigma–Aldrich, 99%). This colloidal suspension was then heated to 363 K (at 0.167 K s^{-1}) and held for 20 h while stirring (12 Hz). The powders were recovered by vacuum filtration and washed with deionized water until the filtrate pH was 7, treated in ambient stagnant air at 383 K for 20 h, and then heated in flowing dry air (99.999%, 1.67 $cm^3\ g^{-1}\ s^{-1}$, Praxair) to 723 K (at 0.167 K s^{-1}) and held for 5 h. These samples were treated in flowing 10% H_2/He (99.999%, 5.56 $cm^3\ g^{-1}\ s^{-1}$, Praxair) by heating to 573 K (at 0.033 K s^{-1}) and held for 2 h, and passivated in flowing 1% O_2/He mixtures (99.999%, 0.83 $cm^3\ g^{-1}\ s^{-1}$, Praxair) at ambient temperature for 1 h before exposure to ambient air.

Metallic Cu particles in the resulting Cu/SiO_2 catalysts were identified using powder X-ray diffraction (XRD) measurements (Cu Kα radiation, $\lambda = 0.15418$ nm, 40 kV, 40 mA, Bruker D8 Advance; diffractogram in Supporting information (SI)). The mean crystallite size (d) of Cu was estimated using the Scherrer equation ($d = 0.90 \cdot \lambda \cdot (\beta \cos\theta)^{-1}$), in which β is the full width at half maximum (FWHM) of the diffraction peak at 2θ. For the resulting Cu/SiO_2 catalysts, the d value of Cu was determined to be 7.9 nm based on the strongest Cu diffraction peak from the (1 1 1) plane ($2\theta = 43.3°$) [8].

TiO_2 catalysts, including P25 (TiO_2(P25), 99.8%, 50 $m^2\ g^{-1}$, anatase:rutile = 3:1 mass, Degussa), anatase TiO_2 (TiO_2(a), 99.7%, 240 $m^2\ g^{-1}$, Alfa Aesar), and rutile TiO_2 (TiO_2(r), 99.5%, 160 $m^2\ g^{-1}$, Aldrich), were treated in flowing air (99.999%, 1.67 $cm^3\ g^{-1}\ s^{-1}$, Praxair) by heating to 673 K (at 0.167 K s^{-1}) and holding for 3 h. TiO_2 and Cu/SiO_2 physical mixtures (TiO_2 + Cu/SiO_2, $(Cu/SiO_2)/TiO_2$ = 0.1–2.0 mass) were obtained by crushing and mixing the two catalysts with a mortar and pestle, and then pressed, crushed, and sieved to retain 180–250 μm particles.

2.2. Catalytic rate measurements

TiO_2 and TiO_2 + Cu/SiO_2 mixtures (10–200 mg) were loaded into a quartz tubular reactor with plug-flow hydrodynamics. The loaded amounts were chosen to maintain differential reactant conversions (<10%). These samples were treated in flowing 10% H_2/He (99.999%, 5.56 $cm^3\ g^{-1}\ s^{-1}$, Praxair) by heating to 543 K (at 0.0833 K s^{-1}), holding for 2 h, and then cooling to reaction temperatures (453–523 K) before rate measurements. Temperatures were set with an electronic controller (Watlow, Series 988) and measured with a K-type thermocouple (0.05 cm diameter, 16 cm length, Omega) held at the outer reactor wall.

C_3 oxygenates, including 1-propanol (>99.9%, Sigma–Aldrich), propanal (>97%, Sigma–Aldrich), 2-propanol (>99.5%, Sigma–Aldrich), and acetone (>99.9%, Fisher), were introduced into a He stream (99.999%, Praxair) using a syringe pump (Cole Parmer, 74900 series); all transfer lines after the liquid introduction point were held at 433 K to avoid condensation of reactants and products. He and H_2 flows were metered using electronic mass flow controllers (Porter, Model 201) to vary reactant pressures and space velocities. Isotopic experiments were conducted similarly but using acetone-d_6 (>99.9%, Aldrich) and D_2 (99.8%, Praxair) instead of the respective protium analog.

Concentrations of reactants and products in the effluent were measured by on-line gas chromatography (Agilent 6890). Specifically, oxygenates and hydrocarbons were detected by flame ionization after chromatographic separation in a methyl silicone capillary column (Agilent HP-1, 50 m, 0.32 mm ID; 1.05 µm film); other gaseous species (CO, CO_2, H_2O, and H_2) were separated in a packed column (Agilent Porapak-Q, 4.8 m, 80–100 mesh) and detected by thermal conductivity. Chemical species were identified using known standards and speciation by mass spectrometry after chromatographic separations (HP 5972 GC/MS). Molecular weight (MW), determined by the molecular ion peak in mass spectrometry, was used to estimate the molecular formula of a product. For instance, aldol condensation of alkanals (MW = N) forms α,β-unsaturated carbonyl compounds (MW = 2 N-18), which can be hydrogenated sequentially to alkanals (MW = 2 N-16) and alkanols (MW = 2 N-14). The Reaction rates are reported either as rates per TiO_2 surface area (areal rates) or as rates per surface Ti—O pair site (turnover rates), for which the exposed Ti—O pair sites were measured by the titration methods described next in Section 2.3.

2.3. Titration of surface sites by probe molecules during catalysis

Pyridine (>99.9%, Sigma–Aldrich), 2,6-di-tertbutylpyridine (>97%, Aldrich), propanoic acid (>99.5%, Sigma–Aldrich), and CO_2 (50% CO_2/He, 99.999%, Praxair) were used as titrants to assess the involvement of various types of exposed surface sites in aldol condensation turnovers. In these experiments, acetone (4 kPa) was first introduced on a TiO_2 + Cu/SiO_2 physical mixture (1:1 mass) at 523 K and 40 kPa H_2. After acetone condensation rates reached steady state, the liquid feed was switched to a mixture of acetone (4 kPa) with each liquid titrant (0.005 titrant/acetone molar). The reactants were then switched back to pure acetone (4 kPa) to assess the reversibility of titrant binding. In the case of CO_2 (4 kPa), the titrant was added as a separate gaseous stream after condensation rates reached constant values at 4 kPa acetone. The concentrations of reactants, products and titrants were measured using the chromatographic protocols described above. The number of accessible Ti—O site pairs ($(\text{Ti—O})_s$) for the examined TiO_2 catalysts was determined from the amount of propionic acid required to fully suppress condensation rates, using acid/$(\text{Ti—O})_s$ stoichiometries of 1 for TiO_2(a) and TiO_2(P25) that adsorb carboxylic acids molecularly and 0.5 for TiO_2(r) that adsorbs carboxylic acids dissociatively via bidentate carboxylate modes as revealed from infrared evidence [29]. Specifically, these titrations were carried out at lower reaction temperatures (453 K) to suppress hydrogenation of propionic acid to propanal and 1-propanol on Cu/SiO_2 and subsequent condensation and esterification of these formed products. This consumption of propionic acid during the titration was taken into account by measuring these products formed from propionic acid; this was made possible by the use of an acid for which hydrogenation forms products distinct from the main reactants. The amounts of such products (n_{consume}) and unreacted acid (n_{outlet}) in the effluent were then subtracted from the amount of propanoic acid introduced (n_{inlet}) in order to determine the amount of propanoic acid irreversibly retained by the TiO_2 surfaces (n_{uptake}) as given by

$$n_{\text{uptake}} = n_{\text{inlet}} - n_{\text{outlet}} - n_{\text{consume}} \quad (1)$$

2.4. Density functional theory methods

The most thermodynamically stable and naturally exposed surfaces for TiO_2(a) and TiO_2(r) are the (1 0 1) and (1 1 0) ones, respectively [31], which provide useful models to study catalytic processes on the corresponding oxides [32]. In particular, the local characteristic of catalytically-relevant properties for the Ti and O sites exposed on these surfaces enables oxide clusters as primary models to represent these surfaces [33]. Here Ti_5O_{19} clusters were abstracted from the (1 0 1) surface of bulk anatase crystal structures (tetragonal, $I4_1$/amd, $a = b = 0.378$ nm, $c = 0.949$ nm) [31] and the (1 1 0) surface of rutile crystals (tetragonal, $P4_4$/amd, $a = b = 0.459$ nm, $c = 0.296$ nm) [31] and used as model surfaces in all density functional theory (DFT) calculations (Scheme 1). Eighteen H-atoms were attached to the dangling O-atoms at the periphery of each cluster in order to maintain charge neutrality. The orientation of the O—H bonds was chosen to maintain that of the Ti—O bonds cleaved to form the clusters, so as to avoid extraneous H-bonding interactions at reactant and transition states. The five Ti-atoms and the three inner O-atoms in each $Ti_5O_{19}H_{18}$ cluster were allowed to relax during all geometry optimizations, but the terminal OH groups were frozen to maintain the local coordination environment of each extended parent surface. These clusters are qualified for DFT treatments of aldol condensation on the corresponding TiO_2 surfaces, because of insignificant effects of neighboring atoms upon catalytic properties of Ti—O site pairs [34] and absence of lateral interaction between adsorbed reactants at low surface coverages that are prevalent at examined catalytic conditions as shown in Section 3.4.

DFT simulations of aldol condensation and esterification routes were carried out at the hybrid B3LYP functional level of theory [35] using the Gaussian 09 program [36], the standard 6-311G(d,p) basis set for C, O, and H-atoms [37], and the effective core potential LANL2DZ basis set for Ti-atoms [38]. An ultrafine grid (99,590) was set for numerical integration; the Berny geometry algorithm [39] was selected to optimize structures of reactants, transition states and products involved in each elementary step with convergence criteria of 1.0×10^{-8} Ha for energy and 1.5×10^{-5} Ha Bohr^{-1} for the maximum residual forces on each atom. The optimized structures were confirmed by frequency calculations at the same computational level in order to ensure that they represent a stable energy minima (i.e., no imaginary frequency) or a saddle point for transition states (i.e., one imaginary frequency). The Grimme D3BJ dispersion correction [40] and the counterpoise correction for the basis set superposition error (BSSE) [41] were taken into account in electronic energy calculations. A fitted scaling factor of 0.9682 was applied to revise DFT-derived vibrational frequencies because of the neglected anharmonicity effects in the theoretical treatment [42]; these revised frequencies were used to derive vibrational partition functions based on the rigid rotor harmonic oscillator (RRHO) approximation and to calculate zero-point energy and thermal corrections [43]. Exceptions were made for low-frequency modes (<100 cm^{-1}) of loosely bound adsorbates, for which a free-rotor model was used instead of the RRHO model in order to avoid significant errors in estimation of vibrational partition functions [44]. Local atomic charges were calculated using the natural bond analysis as implemented in the Gaussian 09 program [45].

The affinities of surfaces for OH^- and H^+ gaseous ions were used to probe the acid and basic strengths of exposed acid–base pairs on these TiO_2 surfaces. Hydroxide anion affinity (E_{HA}) for an acid (A) is defined as the energy released upon attachment of a gaseous hydroxide anion (OH^-) onto an isolated A at the surface to form a bound anion (AOH^-):

$$E_{\text{HA}} = E_{\text{AOH}^-} - E_{\text{A}} - E_{\text{OH}^-} \quad (2)$$

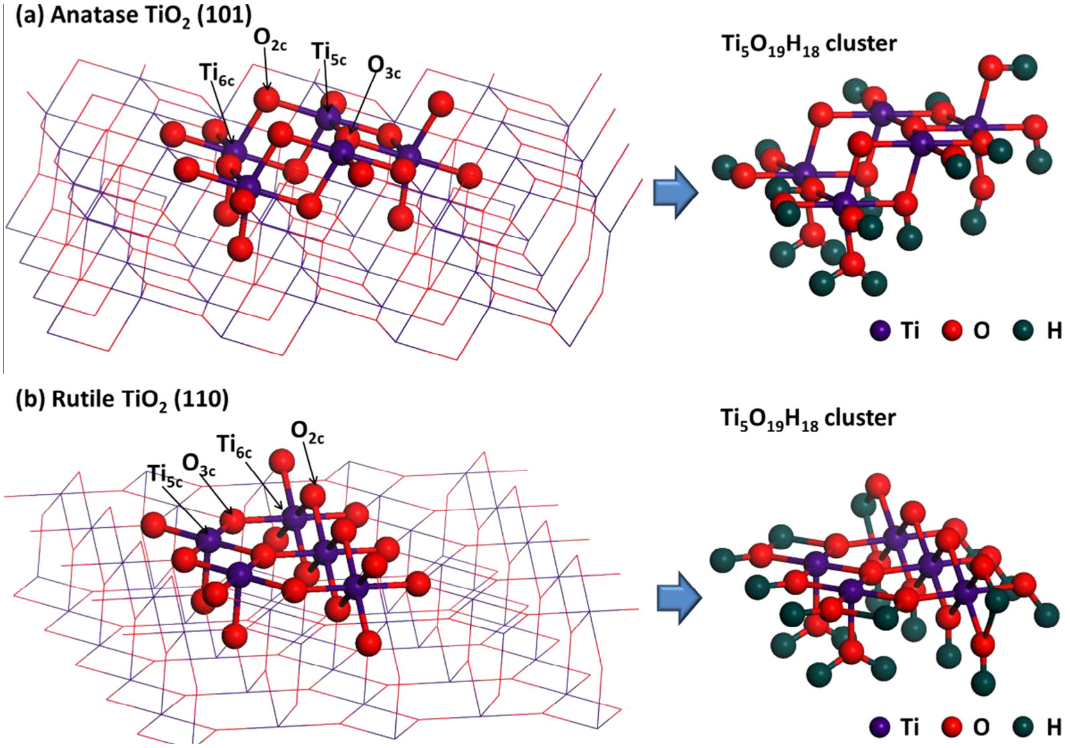

Scheme 1. Structures of $Ti_5O_{19}H_{18}$ clusters abstracted from anatase TiO_2 (1 0 1) and rutile TiO_2 (1 1 0) surfaces.

where E_i represents the electronic energy of species i. Similarly, the proton affinity (E_{PA}) for a base (B) is defined as the energy released upon attachment of a gaseous proton (H^+) onto an isolated B at the surface to form a bound cationic moiety (HB^+):

$$E_{PA} = E_{HB^+} - E_B - E_{H^+} \tag{3}$$

where E_i represents the electronic energy of species i. E_{HA} and E_{PA} are used here as descriptors for acid and basic strengths of Lewis centers, respectively. These affinities of the Ti and O sites exposed on $Ti_5O_{19}H_{18}$ clusters were determined using the above calculation protocols but with the standard 6-311+G(d,p) basis set for the O and H-atoms, because these more diffuse functions are required to accurately describe these charged systems [46].

3. Results and discussion

3.1. C_3 oxygenate reactions on TiO_2 and Cu—TiO_2 catalysts

TiO_2(P25) is used here to examine rates, selectivities, and deactivation rates in reactions of C_3 oxygenates on TiO_2 and Cu—TiO_2 catalysts, but the trends and conclusions are similar, except for differences in reactivity, for TiO_2(a) and TiO_2(r) catalysts, as discussed later. TiO_2(P25), a $TiCl_4$ flame hydrolysis product, consists of a physical mixture of anatase (TiO_2(a)) and rutile (TiO_2(r)) crystallites with an anatase/rutile mass ratio of ~3 [47,48]. The mean diameters of the TiO_2(a) and TiO_2(r) crystals in TiO_2(P25), derived from transmission electron micrographs, are 25 and 85 nm, respectively [48], indicating that anatase surfaces are ~10-fold larger than for rutile crystals in TiO_2(P25). Our thermal treatments in air before catalysis (673 K, 3 h) retained these properties, consistent with the higher temperatures required for anatase–rutile transition (~800 K) [49] and with the infrared evidence for the prevalence of undissociated acetic acid, typical of TiO_2(a), instead of acetate species prevalent on TiO_2(r), on TiO_2(P25) surfaces [29]. As shown in Section 3.3, condensation turnovers are much faster on TiO_2(a) than on TiO_2(r), leading to similar areal rates, mechanistic conclusions, and active surfaces for TiO_2(P25) and TiO_2(a) catalysts.

Aldol condensation of propanal on TiO_2(P25) (523 K; 40 kPa H_2, ~20% conversion of propanal) formed 2-methyl-pent-2-enal and C_9 unsaturated alkanals (such as 2,4-dimethyl-hepta-2,4-dienal and its skeletal isomers) at areal rates of 0.066 and 0.017 μmol C-atom $m^{-2}\,s^{-1}$, respectively (Table 1). These molecules are the expected products from primary and secondary propanal condensation events (Scheme 2) [50]. Their unsaturated nature and the absence of 1-propanol, even in the presence of H_2, indicate that TiO_2(P25) cannot catalyze C=C or C=O hydrogenation via either H_2 activation or H-transfer pathways at these reaction conditions.

The approach to equilibrium factor (η_1) for aldol condensation of C_n carbonyl compounds to form C_{2n} unsaturated carbonyls and H_2O is given by

$$2C_nH_{2n}O \overset{K_{aldol}}{\rightleftarrows} C_{2n}H_{4n-2}O + H_2O \tag{4}$$

$$\eta_1 = \frac{P_{C_{2n}H_{4n-2}O} \cdot P_{H_2O}}{P^2_{C_nH_{2n}O}} \cdot \frac{1}{K_{aldol}} \tag{5}$$

where K_{aldol} is the equilibrium constant. The η_1 value was determined to be 0.3 for propanal (at 20% conversion, 523 K; Table 1) using available thermodynamic data (Section S2, SI), indicating that condensation rates are influenced significantly by thermodynamic constraints. Forward condensation rates (r_f) are related to measured rates (r_n) by

$$r_n = r_f(1 - \eta_1) \tag{6}$$

Fig. 1 shows that the areal forward rates for propanal reactions on TiO_2(P25) decreased with time in the semi-logarithmic manner prescribed by first-order deactivation processes with a deactivation constant (k_d) of 0.078 ks^{-1}. An inverse relation between acetaldehyde aldol condensation rates on TiO_2(a) and the concentration of irreversibly-adsorbed residues [22] suggests that site blockage by

Table 1
Reaction rates of propanal and 1-propanol on TiO_2 and on TiO_2 + Cu/SiO_2.[a]

Catalyst	TiO_2	TiO_2 + Cu/SiO_2	TiO_2 + Cu/SiO_2
Reactant	Propanal	Propanal	1-Propanol
Inlet pressure[b] (kPa)	0.18	0.80	0.80
Residence time (m^2_{TiO2} s (mol C-atom)$^{-1}$)	19.5	3.6	3.6
Propanal pressure[c] (kPa)	0.18	0.17	0.16
1-Propanol pressure[c] (kPa)	<0.01	0.63	0.64
Net formation rate[d] (10^{-3} μmol C-atom m^{-2} s^{-1})			
C_6 oligomer[e]	66	91	90
C_9 oligomer[e]	17	15	13
Propyl propionate	<0.1	8	9
Propene	<0.1	1.2	1.5
Propane	<0.1	0.1	0.2
r_n[f] (10^{-3} μmol C-atom m^{-2} s^{-1})	83	106	103
r_f[g] (10^{-3} μmol C-atom m^{-2} s^{-1})	118	106	103
η_1 (propanal)[h]	0.3	<0.01	<0.01
η_2 (1-propanol)[i]	<0.01	1.0	1.0
η_2 (2-methyl-pentanol)[i]	<0.01	0.8	0.9
η_2 (2-methyl-pentan-3-ol)[i]	<0.01	0.9	0.9

[a] TiO_2(P25) or TiO_2(P25) + 20 wt.% Cu/SiO_2 (1:1 mass), 523 K, 40 kPa H_2, ~20% conversion.
[b] Inlet reactant pressure.
[c] Average pressure in the reactor.
[d] Extrapolated exponentially to zero time.
[e] Derived from propanal condensation (Scheme 2).
[f] Net propanal condensation rates.
[g] Forward propanal condensation rates (Eq. (6)).
[h] Approach to equilibrium factor for aldol condensation (Eq. (5)).
[i] Approach to equilibrium factor for hydrogenation to alkanol (Eq. (8)).

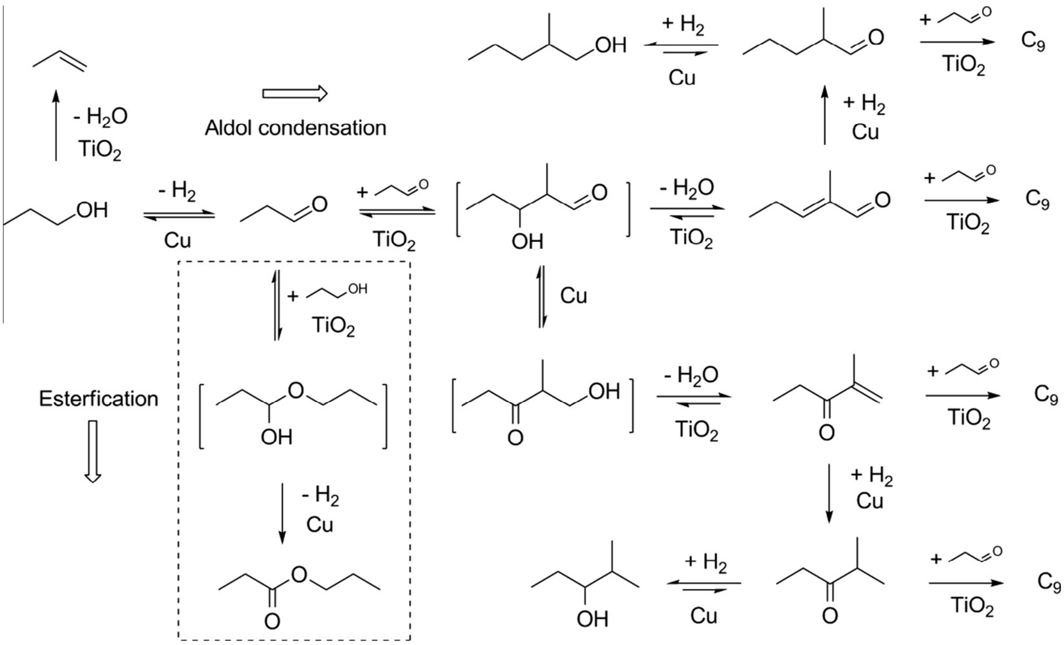

Scheme 2. Reaction network of aldol condensation and esterification for propanal and 1-propanol reactants on TiO_2 and Cu/SiO_2 catalysts. The concentrations of the molecules shown in brackets were below the experimental detection limit (0.001 kPa).

sequential condensation products accounts for the observed deactivation. The ubiquitous thermodynamic constraints and rapid deactivation, taken together, render monofunctional TiO_2 surfaces unsuitable as practical condensation catalysts and also preclude any rigorous kinetic or mechanistic analysis of the elementary states and active sites that mediate such reactions on oxide surfaces.

Propanal reactions were also examined on TiO_2(P25) + Cu/SiO_2 physical mixtures (1:1 mass; 523 K, 40 kPa H_2). Propanal hydrogenation on the Cu function (Scheme 2) led to equilibrated 1-propanol–propanal mixtures, as shown by the approach to equilibrium factor (η_2; Table 1):

$$C_nH_{2n}O + H_2 \overset{K_{hydro}}{\rightleftarrows} C_nH_{2n+1}OH \tag{7}$$

$$\eta_2 = \frac{P_{C_nH_{2n+1}OH}}{P_{H_2} \cdot P_{C_nH_{2n}O}} \cdot \frac{1}{K_{hydro}} \tag{8}$$

where K_{hydro} is the equilibrium constant of the hydrogenation reaction, and obtained from available thermodynamic data (Section S2,

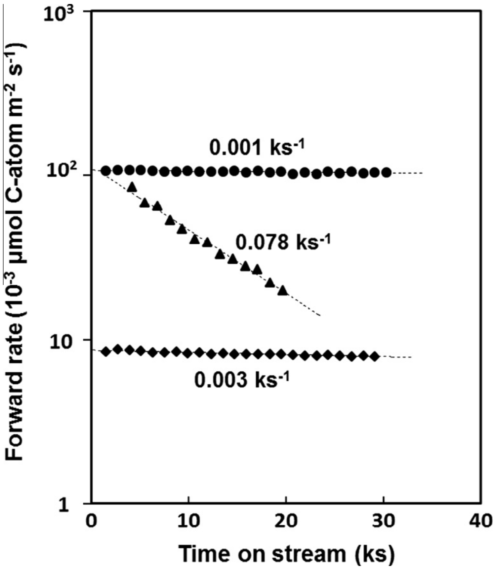

Fig. 1. Time-on-stream profiles for forward rates of aldol condensation (▲) on TiO_2(P25) and for forward rates of aldol condensation (●) and esterification (◆) on TiO_2(P25) + Cu/SiO_2 (1:1 mass) (0.18 kPa average propanal pressure in the reactor, 523 K, 40 kPa H_2). Dashed lines represent exponential regressed fits of the data with first-order deactivation constants shown beside the lines.

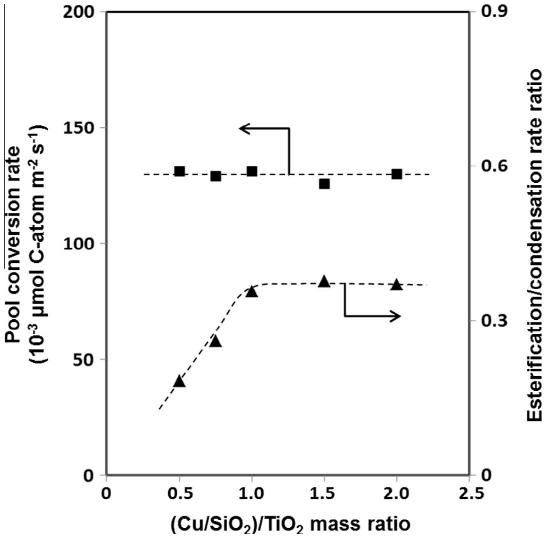

Fig. 2. Effects of $(Cu/SiO_2)/TiO_2$ mass ratios on areal conversion rates of the 1-propanol–propanal reactant pool (■) and on esterification/condensation rate ratios (▲) (TiO_2(P25) + 20 wt.% Cu/SiO_2, 523 K, 0.8 kPa 1-propanol, 40 kPa H_2). Dashed curves indicate trends. Areal rates are given on the basis of TiO_2 surface areas.

SI). These equilibrated mixtures can be rigorously treated as a reactant chemical lump in all kinetic analyses. Their kinetic equivalence is evident from the identical aldol condensation and esterification rates measured at a given propanal pressure when using either 1-propanol or propanal as the inlet reactant (0.8 kPa reactant; 40 kPa H_2; Table 1). Henceforth, conversions and selectivities are based on the formation of products from this equilibrated reactant lump. Cu surfaces can catalyze aldol condensation and esterification of 1-propanol–propanal reactants [50], which form products identical to those observed on TiO_2(P25) + Cu/SiO_2 mixtures (Table 1). These rates on Cu surfaces, however, are >10-fold lower than those on TiO_2(P25) catalysts at all conditions used here; such Cu contributions were subtracted from reported rates on TiO_2(P25) + Cu/SiO_2 mixtures when so required. Areal conversion rates of 1-propanol–propanal reactants on TiO_2(P25) did not depend on the amount of Cu present in these physical mixtures (0.5–2.0 $(Cu/SiO_2)/TiO_2$ mass ratio; Fig. 2), consistent with the ability of the Cu function to fully and quickly equilibrate alkanol–alkanal mixtures at the prevalent H_2 pressures and with the sole kinetic relevance of TiO_2-catalyzed condensation and esterification steps.

C_6 and C_9 condensation products also formed from 1-propanol–propanal reactants on TiO_2(P25) + Cu/SiO_2, even at low conversions (12–20%). They consist of hydrogenated forms of the condensation products observed on TiO_2(P25). For instance, 2-methyl-pent-2-enal was hydrogenated to 2-methyl-pentanal and 2-methyl-pentanol, and to their respective isomers (2-methyl-pentan-3-one and 2-methyl-pentan-3-ol) (Scheme 2) to form equilibrated mixtures at each H_2 pressure on TiO_2(P25) + Cu/SiO_2 mixtures with their corresponding approach to equilibrium constants close to unity (Table 1). The hydrogenation of 2-methyl-pent-2-enal, the primary propanal condensation product, circumvents the thermodynamic bottlenecks prevalent on TiO_2 catalysts, thus rendering condensation reactions essentially irreversible ($\eta_1 < 0.01$, Table 1) and leading to higher areal conversion rates (r_n: from 0.083 to 0.106 µmol C-atom m^{-2} s^{-1}; Table 1). These areal rates, when corrected by their approach to equilibrium, become the same on the monofunctional TiO_2(P25) and on the bifunctional mixture. The presence of the Cu function led to a marked decrease in first-order deactivation constants (k_d) from 0.078 to 0.001 ks^{-1} (Fig. 1), seemingly as the result of the scavenging of the unsaturated products typically implicated in the formation of unreactive residues that block active sites on TiO_2 surfaces.

Propyl propionate was not detected during propanal reactions on TiO_2(P25), but formed from the equilibrated 1-propanol–propanal mixtures prevalent on TiO_2(P25) + Cu/SiO_2. Esterification/condensation rate ratios increased from 0.16 to 0.36 with increasing the $(Cu/SiO_2)/TiO_2$ ratio (0.5–1.0) and then reached a constant value for ratios larger than unity (Fig. 2). Pool conversion rates (the combined esterification and condensation rates), however, were unaffected by the amount of Cu/SiO_2 in the physical mixture (Fig. 2). These data suggest that the Cu function is required also to complete esterification turnovers and that the Cu surface area required to remove thermodynamic or kinetic bottlenecks exceeds those required for condensation routes. The constant conversion rates, however, indicate that condensation and esterification turnovers share a common intermediate, formed in the kinetically-relevant step, which is subsequently involved in condensation and esterification events that determine selectivity, but not alkanol–alkanal pool conversion turnover rates. We surmise here, and confirm later by kinetic, isotopic, and theoretical methods, that unstable hemiacetals form via reactions of alkanols with alkanal-derived enolate species [51], with the latter formed in the kinetically-relevant step; such reactions are disfavored by thermodynamics, but dehydrogenation to more stable esters on Cu scavenges the products to form more stable esters, thus rendering such reactions first reversible, leading to higher esterification to condensation ratios, and ultimately irreversible and no longer consequential for selectivity at higher Cu contents (Fig. 2). The constant ratios at high Cu contents ($(Cu/SiO_2)/TiO_2 \geqslant 1.0$, Fig. 2) rigorously reflect the respective kinetic rates of alkanol and alkanal reactions with enolates and thus the intrinsic reactivity of TiO_2 surfaces in such reactions, as discussed in detail in Section 3.4.

Acetone condensation reactions were also examined on TiO_2(P25) and TiO_2(P25) + Cu/SiO_2 mixtures (523 K; 40 kPa H_2). Primary condensation events led to equilibrated mixtures of 4-methyl-pent-3-en-2-one (mesityl oxide) and 4-methyl-pent-4-en-2-one (isomesityl oxide) and to secondary C_9 alkanone products (e.g., 4,6-dimethyl-hepta-3,5-dien-2-one and its skeletal isomers; Scheme 3); the presence of Cu/SiO_2 and H_2 rendered acetone reactants and the unsaturated condensation products present in

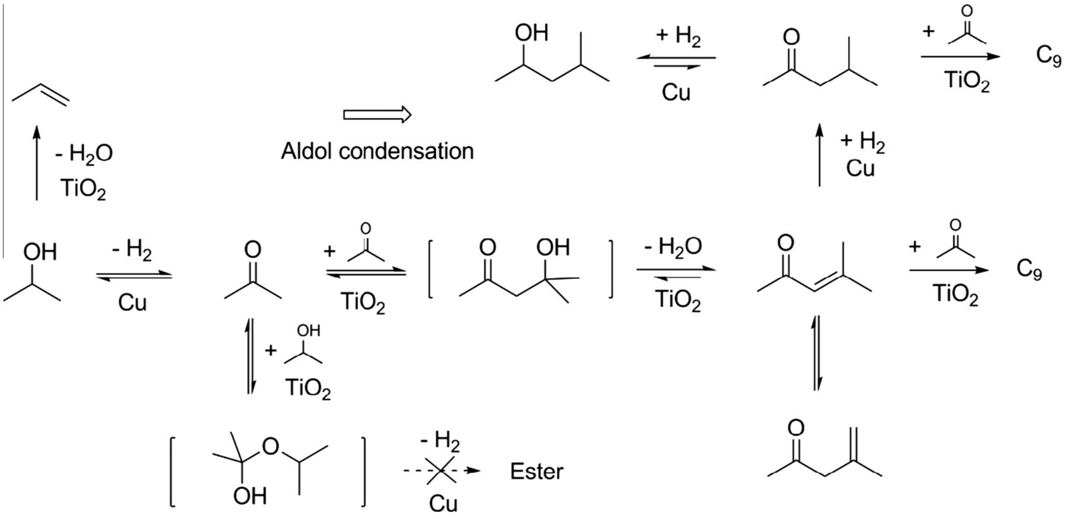

Scheme 3. Reaction network of aldol condensation for acetone and 2-propanol reactants on TiO_2 and Cu/SiO_2 catalysts. The concentrations of the molecules shown in brackets were below the experimental detection limit (0.001 kPa).

Table 2
Reaction rates of acetone and 2-propanol on TiO_2 and on $TiO_2 + Cu/SiO_2$.[a]

Catalyst	TiO_2	$TiO_2 + Cu/SiO_2$	$TiO_2 + Cu/SiO_2$
Reactant	Acetone	Acetone	2-Propanol
Inlet pressure[b] (kPa)	0.70	0.80	0.80
Residence time (m^2_{TiO2} s (mol C-atom)$^{-1}$)	1.8	2.1	2.1
Acetone pressure[c] (kPa)	0.70	0.72	0.71
2-Propanol pressure[c] (kPa)	<0.01	0.08	0.09
Net formation rate[d] (10^{-3} μmol C-atom m^{-2} s^{-1})			
C_6 oligomer[e]	261	343	345
C_9 oligomer[e]	220	210	202
Propene	<0.1	80	93
Propane	<0.1	4.2	4.8
r_n[f] (10^{-3} μmol C-atom m^{-2} s^{-1})	481	553	547
r_f[g] (10^{-3} μmol C-atom m^{-2} s^{-1})	534	553	547
η_1 (acetone)[h]	0.1	<0.01	<0.01
η_2 (2-propanol)[i]	<0.01	1.0	1.0
η_2 (4-methyl-pentan-2-ol)[i]	<0.01	1.0	0.9

[a] TiO_2(P25) or TiO_2(P25) + 20 wt.% Cu/SiO_2 (1:1 mass), 523 K, 40 kPa H_2, ~20% conversion.
[b] Inlet reactant pressure.
[c] Mean pressure in the reactor.
[d] Extrapolated exponentially to zero time.
[e] Derived from acetone condensation (Scheme 3).
[f] Net acetone condensation rates.
[g] Forward acetone condensation rates (Eq. (6)).
[h] Approach to equilibrium factor for aldol condensation (Eq. (5)).
[i] Approach to equilibrium factor for hydrogenation to alkanol (Eq. (8)).

equilibrium with their saturated analogs, as described below. For instance, 4-methyl-pentan-2-one and 4-methyl-pentan-2-ol formed are in equilibrium with each other and with mesityl oxide (Scheme 3).

Acetone condensation rates on TiO_2(P25) were affected by equilibrium constraints ($\eta_1 = 0.1$, 523 K, 0.8 kPa acetone; Table 2) and decreased rapidly with time on stream ($k_d = 0.14$ ks^{-1}; Fig. 3). Equilibrium constraints were negligible on TiO_2(P25) + Cu/SiO_2 ($\eta_1 < 0.01$; Table 2), however, and deactivation was essentially suppressed ($k_d = 0.002$ ks^{-1}; Fig. 3). The Cu function also enabled the formation of equilibrated 2-propanol–acetone reactants ($\eta_2 = 1$; Table 2), resulting in identical condensation rates for pure acetone and 2-propanol reactants at each given acetone pressure, set by 2-propanol–acetone-H_2 equilibration (0.8 kPa reactant; 40 kPa H_2; Table 2). Esters were not detected among the products of 2-propanol–acetone reactants, because the OH group in hemiacetals resides at a tertiary C-atom (Scheme 3), thus precluding dehydrogenation to form an ester.

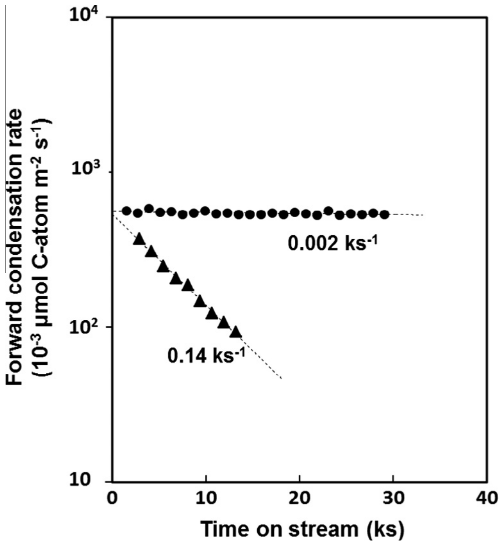

Fig. 3. Forward rates of aldol condensation as a function of time-on-stream on TiO_2(P25) (▲) and on TiO_2(P25) + Cu/SiO_2 (●) (0.70 kPa average acetone pressure in the reactor, 523 K, 40 kPa H_2). Dashed lines represent exponential regressed fits of the data with first-order deactivation constants shown next to each data set.

In summary, the presence of Cu as a hydrogenation–dehydrogenation function and of H_2 did not influence forward conversion rates of propanal or acetone on TiO_2 surfaces, but led to higher measured rates by scavenging primary enal or enone products to more saturated ones (e.g. C_6 alkanals, alkanones, and alkanols); these reactions also suppressed the formation of larger unsaturated molecules that form unreactive residues, thus inhibiting deactivation to nearly undetectable levels. The rapid equilibration of alkanol–alkanal (alkanone) mixtures renders the two molecules indistinguishable in condensation reactions.

3.2. Equivalence of alkanols and alkanones/alkanals and oxygen removal and chain growth at practical conversions

Here, we show that alkanol streams can be converted to products with longer C-chains and lower oxygen content via condensation and esterification reactions on bifunctional TiO_2(P25) + Cu/SiO_2

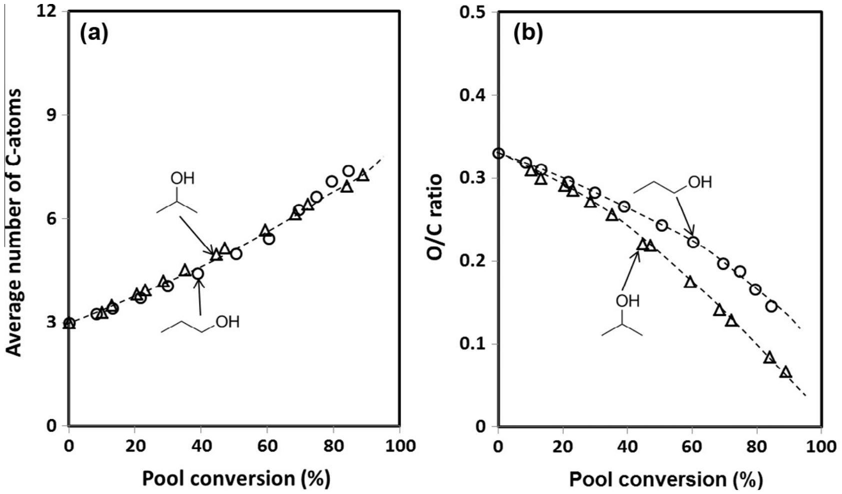

Fig. 4. Average number of C-atoms (a) and O/C ratio (b) of liquid effluents as a function of alkanol–alkanal (alkanone) pool conversions for pure 1-propanol (○) and 2-propanol (Δ) reactant feeds (TiO_2(P25) + 20 wt.% Cu/SiO_2 (1:1 mass), 523 K, 0.8 kPa 1-propanol or 2-propanol, 40 kPa H_2). Dashed curves indicate trends.

catalysts at practical conversions. The average number of C-atoms of the effluent stream (including unreacted lumped reactants) increased from 3.0 (1-propanol) to 7.4 as the conversion of the lumped (equilibrated) 1-propanol–propanal reactants increased to 84% (523 K; 40 kPa H_2; Fig. 4a); the O/C ratio in the molecules present in the effluent stream decreased from 0.33 (in 1-propanol) to 0.15 (Fig. 4b). The products present at all conversions and the trends in Fig. 4 are consistent with the C—C and C—O bond formation and O-removal steps characteristic of condensation and esterification reactions (Scheme 2). Similar results for 2-propanol reactants are shown in Fig. 4 and elsewhere for C_2–C_5 alkanols [29]; the conclusions, practical consequences, and catalyst requirements apply broadly to conversion strategies for alkanols and carbonyl compounds and their mixtures, which are ubiquitous in biomass-derived streams.

These bifunctional strategies, however, are much less effective when noble metals (e.g. Pt and Pd) are used instead of Cu as the metal function, because their higher decarbonylation activity leads to the concurrent formation of CO, which adsorbs strongly and inhibits the metal function [52]. Cu surfaces, in contrast, do not catalyze decarbonylation to detectable extents and would, in any case, adsorb CO much more weakly, making it the most effective and least costly choice as the metal function in these cascade reaction strategies.

3.3. Site requirements of aldol condensation on TiO_2 surfaces

Rigorous mechanistic assessments of elementary steps and site requirements require a reliable measure of the number and the chemical properties of plausible active sites on TiO_2 surfaces. These site counts can then be used to express reactivity in terms of turnover rates, thus allowing comparisons among surfaces differing in chemical composition or crystallographic exposure; they also make it possible to compare free energies derived from theory and experiment in attempts to choose among alternate mechanistic hypotheses. Such site counts require, in turn, that we titrate surface sites with molecules showing different affinities for the various types of sites prevalent on oxides (Lewis and Brønsted acids, bases) in order to assess their abundance and their involvement in catalytic turnovers.

Fig. 5 compares areal acetone condensation rates on TiO_2(P25), pure TiO_2(a) and pure TiO_2(r) (503 K; 0.6 kPa acetone; 40 kPa H_2), all present as physical mixtures with Cu/SiO_2. TiO_2(P25) and TiO_2(a) showed similar stability (k_d 0.004 and 0.006 ks^{-1}, respectively) and areal rates (0.146 and 0.161 μmol C-atom m^{-2} ks^{-1}, respectively); TiO_2(r), in contrast, exhibited much faster deactivation (k_d 0.059 ks^{-1}) and lower initial rates (0.025 μmol C-atom m^{-2} ks^{-1}). The similar behavior of TiO_2(P25) and TiO_2(a) and the much lower reactivity of TiO_2(r) show that anatase surfaces predominantly account for condensation turnovers. It seems plausible that measured rates on TiO_2(r) may reflect, in fact, anatase-like surfaces on some rutile crystallites or the presence of small crystals of TiO_2(a) [29,49], undetectable by X-ray diffraction, but contributing disproportionately to surface areas in TiO_2(P25). DFT treatments confirmed that activation barriers for aldol condensation are much larger on TiO_2(r) than on TiO_2(a) surfaces (Section S8, SI).

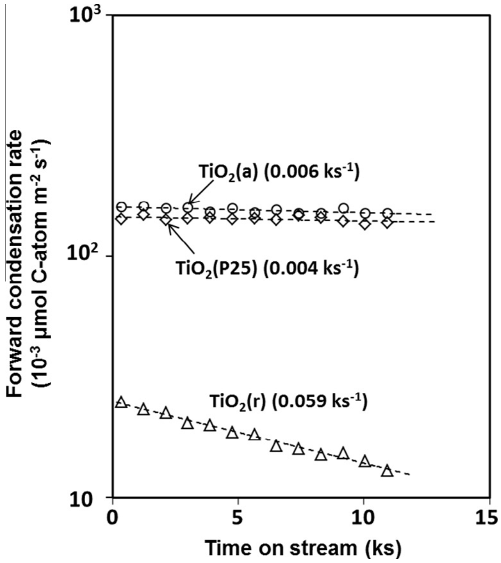

Fig. 5. Areal forward acetone condensation rate as a function of time-on-stream on TiO_2(P25), TiO_2(a) and TiO_2(r) at 503 K (TiO_2 + 20 wt.% Cu/SiO_2 (1:1 mass), 0.6 kPa acetone, 40 kPa H_2). Dashed lines represent exponential regressed fits of the data with first-order deactivation constants shown next to each data set.

Site titrations using probe molecules that bind selectively to acid or basic surface sites were carried out to determine their respective surface densities and the extent to rates which are influenced by their binding on TiO_2(P25). CO_2 [13], 2,6-di-tert-butylpyridine (DTBP) [53], pyridine [12], and propanoic acid [12] were chosen as titrants for basic sites, Brønsted acid sites, Lewis acid sites, and acid–base site pairs, respectively. Each titrant was introduced together with acetone (4 kPa) on TiO_2(P25) + Cu/SiO_2 (1:1 mass) at 523 K and 40 kPa H_2; Cu did not influence titrant uptakes or cause significant chemical conversions of these titrants to other species.

CO_2, even at high concentrations (4 kPa; CO_2/acetone = 1.0), did not detectably influence reaction rates (Fig. 6), indicating that strong basic sites are not involved in condensation turnovers. DTBP (DTBP/acetone = 0.005) also did not affect rates (Fig. 6), showing that Brønsted acid sites are not involved. In contrast, pyridine (pyridine/acetone = 0.005) decreased rates slightly from 2.2 to 1.8 μmol C-atom m^{-2} s^{-1} (Fig. 6); rates gradually recovered, however, upon pyridine removal (over ~3 ks; Section S3, SI). Thus, weak Lewis acid sites that reversibly bind pyridine appear to be required for condensation turnovers.

Propanoic acid strongly decreased condensation rates (2.2–0.6 μmol C-atom m^{-2} s^{-1} (Fig. 6), even at concentrations much lower than for acetone reactants (propanoic acid/acetone = 0.005); such inhibition was gradually and fully reversed, but over periods (~8 ks; Section S3, SI) much longer than typical turnover times. Infrared spectra show that carboxylic acids bind on TiO_2(a) surfaces without dissociation via concerted interactions between their carbonyl O-atom and a Ti center and between their acidic H-atom and a vicinal O-atom on TiO_2 surfaces [29]. These propanoic acid inhibition effects are much stronger (and much more slowly reversed) than for pyridine titrants, indicating that acid–base Ti—O site pairs are likely to account for the reactivity of TiO_2(a) surfaces. In this context, basic O-atoms act as H-abstractors, required to activate α-C—H bonds in the alkanal (alkanone) reactants [25], with Ti-atoms acting to stabilize the transition state that mediate enolate formation in the kinetically-relevant elementary step via interactions with the carbonyl group in the alkanal (alkanone) reactants.

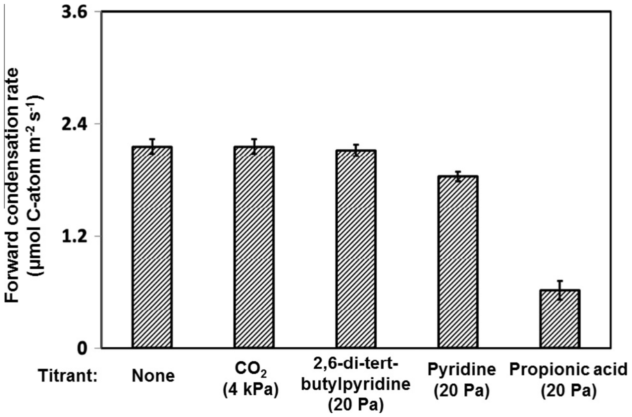

Fig. 6. Effects of CO_2, 2,6-di-tert-butylpyridine, pyridine, and propanoic acid introductions on areal forward acetone condensation rates on TiO_2(P25) + 20 wt.% Cu/SiO_2 (1:1 mass) at 523 K (4 kPa acetone, 4 kPa CO_2, 20 Pa 2,6-di-tert-butylpyridine, 20 Pa pyridine, 20 Pa propanoic acid, 40 kPa H_2).

The strong interactions of propanoic acid with acid–base site pairs on TiO_2 allow measurements of the number of such sites at TiO_2 surfaces during acetone condensation catalysis. In doing so, we use lower reaction temperatures (453 K) to ensure irreversible binding and to suppress any hydrogenation of propionic acid to propanal or 1-propanol and subsequent condensation and esterification of these formed products. The number of bound acid molecules was determined by accounting for trace amounts of such products formed from propionic acid that are chemically distinct from those formed from acetone reactants, and of unreacted acid in the effluent (Section 2.3).

Areal acetone condensation rates on TiO_2(P25) decreased almost linearly with the amount of adsorbed propanoic acid (Fig. 7a). Slight deviations from these linear trends reflect the growing scarcity of vicinal Ti centers, required for C—C coupling steps (Section 3.4), as Ti—O site pairs are titrated by propanoic acid. These data show that Ti—O site pairs are titrated stoichiometrically and irreversibly by propanoic acid and that such sites are involved in the kinetically-relevant elementary steps that mediate aldol condensation reactions.

The number of titrants required to fully suppress condensation rates (by linear extrapolation of the data in Fig. 7) gives the number of Ti—O pairs on each surface. Their number on TiO_2(P25) (3.7 titrants nm^{-2}, Fig. 7a) is slightly smaller than the number of Ti—O site pairs determined from the anatase crystal structure for its low-index planes (5.2 nm^{-2}, (101); 5.6 nm^{-2}, (100); 7.0 nm^{-2}, (001)), plausibly because of the presence of some permanent OH groups, required to preserve favorable O and Ti coordination on surfaces of small crystallites [29].

Propanoic acid titration data were also measured on TiO_2(a) and TiO_2(r). The number of site pairs (per surface area) was nearly identical in TiO_2(a) (4.0 titrants nm^{-2}, Fig. 7b) and TiO_2(P25)

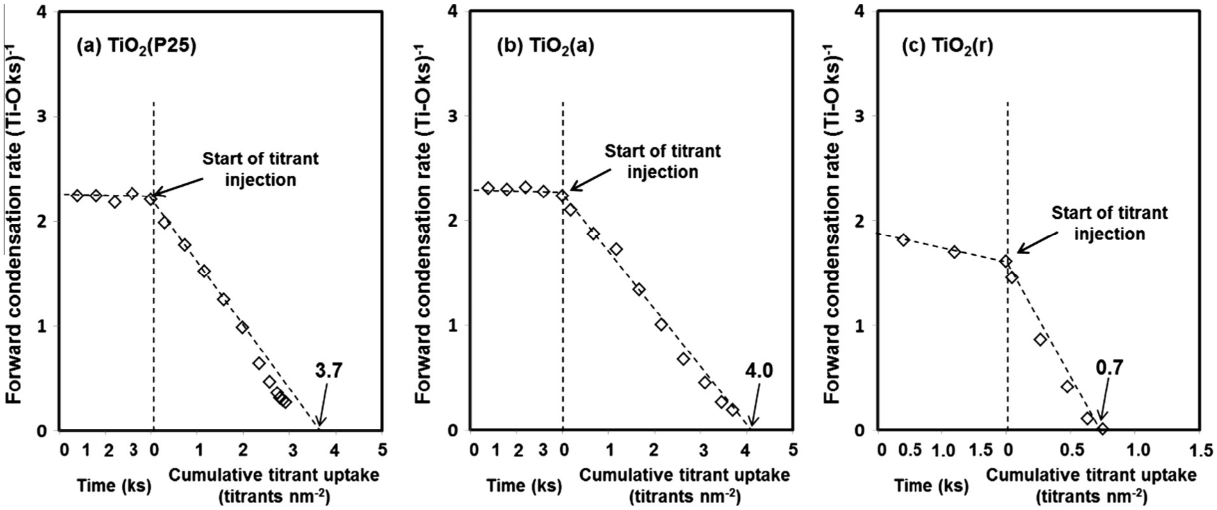

Fig. 7. Forward acetone condensation rates on (a) TiO_2(P25), (b) TiO_2(a), and (c) TiO_2(r) at 453 K before propanoic acid introduction (vs. time) and after (vs. cumulative titrant uptake) (TiO_2 + 20 wt.% Cu/SiO_2 (1:1 mass), 0.8 kPa acetone, 20 Pa propanoic acid, 20 kPa H_2). The rates are normalized by surface Ti—O site pairs measured from titration with propanoic acid. Dashed lines are linear regression fits.

(3.7 titrants nm^{-2}, Fig. 7a), consistent with the prevalence of anatase surfaces in TiO_2(P25) [47,48]. Site densities on TiO_2(r) (0.7 titrants nm^{-2}, Fig. 7c), however, were much smaller than on anatase and also than those expected from the rutile crystal structure (5.2 nm^{-2}, (1 1 0); 7.4 nm^{-2}, (1 0 0); 8.0 nm^{-2}, (0 1 1)). We surmise that such low densities of accessible Ti—O site pairs reflect the placement of unreactive acetone-derived species during acetone reactions before titrant introduction; such species prevent access to sites for dissociating OH bonds in propanoic acid or α-C—H bonds in acetone, a conclusion consistent with the faster deactivation of TiO_2(r) surfaces and with DFT treatments that implicate strong acid–base site pairs on TiO_2(r) in the difficult reprotonation and desorption of the C—C coupling products (Section S8, SI). Initial acetone turnover rates (normalized by the number of catalytically-relevant acid–base site pairs) are similar on TiO_2(r) (1.9 (Ti—O ks)$^{-1}$, Fig. 7c), TiO_2(P25) (2.2 (Ti—O ks)$^{-1}$, Fig. 7a) and TiO_2(a) (2.3 (Ti—O ks)$^{-1}$, Fig. 7b). These data are consistent with condensation turnovers that occur exclusively on anatase surfaces, making turnover rates and site densities on TiO_2(r) merely a consequence of anatase-like surfaces present as minority species.

Taken together, these assessments of the number and type of active sites during catalysis indicate that Ti—O acid–base site pairs of intermediate acid and basic strengths on anatase surfaces are required for efficient condensation turnovers. This evidence and the ability to determine intrinsic site reactivities allow theoretical treatments based on the posited site structures, as well as the accurate benchmarking of DFT-derived activation free energies against measured values, while also providing confirmatory evidence for the kinetic relevance of the proposed elementary steps (Section 3.5).

3.4. Kinetic dependence of condensation and esterification reactions and consequences for the kinetic relevance of elementary steps

The effects of propanal and 1-propanol pressures on aldol condensation and esterification rates were examined on TiO_2(P25) + Cu/SiO_2 physical mixtures (1:1 mass; 523 K). 1-Propanol–propanal-H_2 equilibration was achieved at all reaction conditions (Fig. 8a). The condensation products (Scheme 2) contain new C—C bonds formed exclusively at the α-C position in one of the propanal reactants, as expected from enolate-like intermediates formed via α-H abstraction and their subsequent nucleophilic attack on another propanal, a characteristic of aldol condensations catalyzed by strongly basic oxides or liquid bases [1,12].

Fig. 8a shows that combined turnover rates (per Ti—O pair) for the conversion of 1-propanol–propanal reactants to condensation and esterification products are proportional to propanal pressure, but insensitive to 1-propanol pressure. The ratio of esterification to condensation rates, however, depends linearly on the 1-propanol/propanal ratio present in the equilibrated reactants (Fig. 8b). These trends indicate that the formation of common enolate-like species from propanal limits the combined formation rates of condensation and esterification products as described in Section 3.1. Moreover, the insensitivity of conversion rates to 1-propanol concentrations indicates that reactions of enolates to form new C—C or C—O bonds cannot be kinetically-relevant, because their rates would differ for the reactions of these enolates with alkanols (to form hemiacetals/esters) and with alkanals (to form aldols), thus rendering conversion rates dependent on both alkanol and alkanal pressures. We conclude, therefore, that enolate formation must be the sole kinetically-relevant step, with product selectivities determined by the relative reactivity of enolates with alkanols and alkanals and by their respective pressures, consistent with DFT-derived barriers reported below (Section 3.5).

Scheme 4 depicts condensation and esterification elementary steps consistent with these kinetic effects on rates and selectivities. The kinetically-relevant formation of an enolate from propanal via α-C—H bond cleavage occurs irreversibly on Ti—O site pairs that remain sparsely covered during catalysis; at such sites, the lattice O-atoms act as the base and the Ti centers act as the Lewis acid centers that bind the O-atom in the enolate formed (Step 2; Scheme 4). These enolates then couple with a propanal bound at a vicinal Ti center to form a C—C bond (Step 4; Scheme 4) and the aldol species dehydrate to form α,β-unsaturated carbonyl products (Steps 6 and 7; Scheme 4). These enolates can also react with a 1-propanol bound at the vicinal Ti center to form a C—O bond via an equilibrated H-shift between the enolate and 1-propanol (Step 9; Scheme 4) and a subsequent C—O coupling reaction between the resulting propanal and alkoxide species to form a hemiacetal (Step 10; Scheme 4), as suggested by DFT treatments (Section 3.5). Propyl propionate is finally formed via dehydrogenation of the OH group in the hemiacetals on the Cu function (Step 13; Scheme 4).

The elementary steps in Scheme 4 lead to an equation for the enolate formation turnover rate:

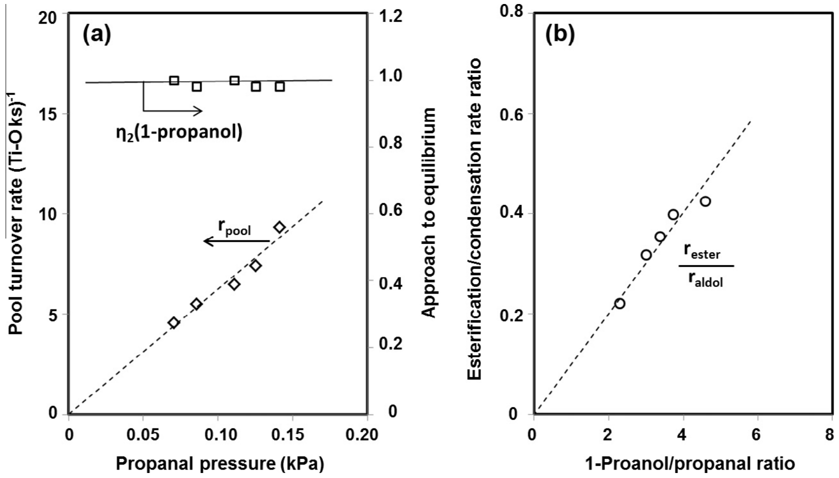

Fig. 8. Effects of propanal pressure on turnover rates for the conversion of 1-propanol–propanal equilibrated reactants (a) and of 1-propanol/propanal ratio on esterification to condensation rate ratios (b) (TiO_2(P25) + 20 wt.% Cu/SiO_2 (1:1 mass), 523 K, 0.8 kPa 1-propanol, 10–80 kPa H_2). Dashed lines in (a) and (b) represent the regressed fits to the functional forms of Eqs. (10) and (16), respectively. The solid line in (a) represents a linear regression fit.

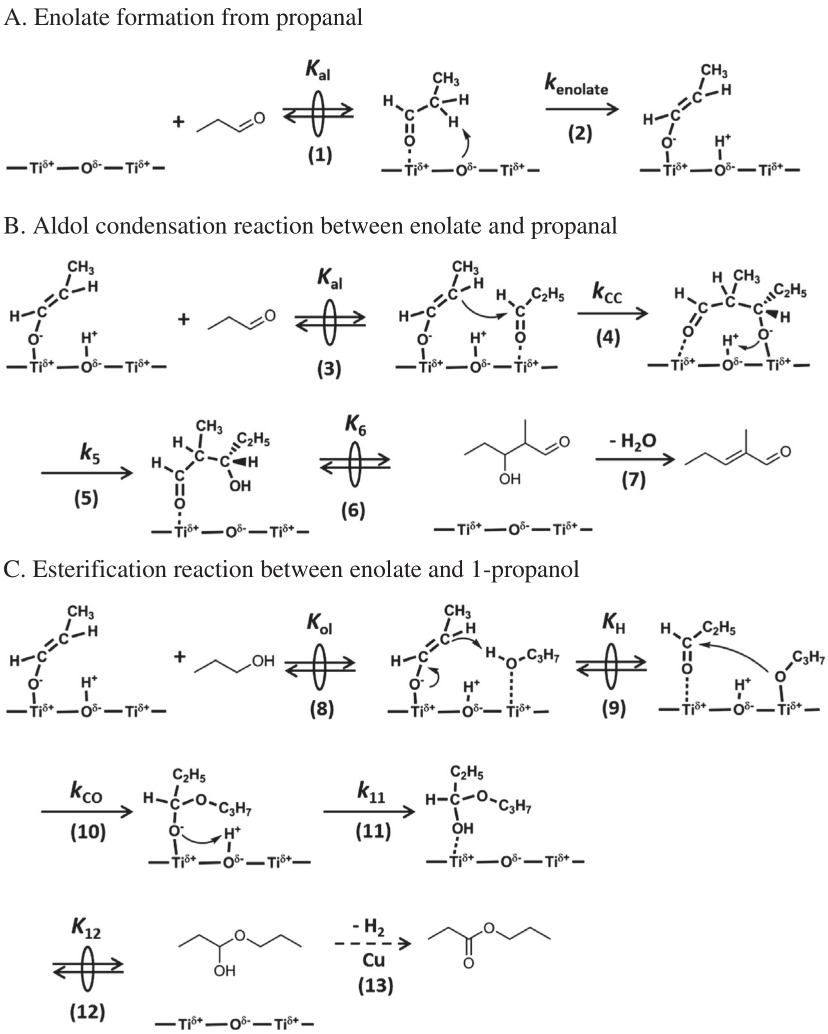

Scheme 4. Aldol condensation and esterification reaction pathways, illustrated here for 1-propanol–propanal reactants, on bifunctional TiO_2 + Cu/SiO_2 catalysts. Steps occurring on Ti—O site pairs and on Cu surfaces are represented by solid and dashed arrows, respectively. Reaction numbers used throughout the text are in parentheses (e.g., (1)) below each reaction arrow; k_j and K_j are kinetic constant of the forward step and equilibrium constant for Step j, respectively.

$$\frac{r_{\text{enolate}}}{[L]_{\text{TiO2}}} = \frac{r_{\text{aldol}} + r_{\text{ester}}}{[L]_{\text{TiO2}}} = \frac{k_{\text{enolate}} K_{\text{al}} P_{\text{propanal}}}{1 + \sum K_i P_i} \tag{9}$$

where $[L]_{\text{TiO2}}$ is the number of active Ti—O site pairs, r_{enolate}, r_{aldol}, and r_{ester} are the respective enolate formation, aldol condensation, and esterification rates, k_{enolate} is the rate constant for enolate formation from propanal, and K_i is adsorption constant for species i on Ti—O site pairs (e.g., propanal (K_{al}), 1-propanol (K_{ol}) and products). The first-order dependence of r_{enolate} on propanal pressure indicates that $\sum(K_i P_i)$ is much smaller than unity and that TiO_2 surfaces, lacking strong basic or acid sites, are essentially bare during reactions of equilibrated alkanal–alkanol mixtures. As a result, measured rates are accurately described by

$$\frac{r_{\text{enolate}}}{[L]_{\text{TiO2}}} = k_{\text{enolate}} K_{\text{al}} P_{\text{propanal}} = k'_{\text{enolate}} P_{\text{propanal}} \tag{10}$$

where k'_{enolate} represents the apparent first-order rate constant for enolate formation.

The formalism of transition state theory allows these rates to be related to an activation free energy ($\Delta G'^{\ddagger}_{\text{enolate}}$; derivation details in Section S4, SI):

$$\frac{r_{\text{enolate}}}{[L]_{\text{TiO2}}} = \frac{k_B T}{h} e^{-\frac{\Delta G'^{\ddagger}_{\text{enolate}}}{RT}} P_{\text{propanal}} \tag{11}$$

which is related, in turn, to k'_{enolate} through

$$\Delta G'^{\ddagger}_{\text{enolate}} = -RT \ln\left(\frac{h}{k_B T} k'_{\text{enolate}}\right) \tag{12}$$

$\Delta G'^{\ddagger}_{\text{enolate}}$ represents the difference between the free energy of the transition state (TS) for enolate formation ($G^{\ddagger}_{\text{enolate}}$) and of a gaseous carbonyl reactant (G_{carbonyl}; propanal in this case) and a bare Ti—O site ($G_{\text{Ti—O}}$) as shown in Scheme 5:

$$\Delta G'^{\ddagger}_{\text{enolate}} = G^{\ddagger}_{\text{enolate}} - G_{\text{carbonyl}} - G_{\text{Ti—O}} \tag{13}$$

The measured values of k'_{enolate} and $\Delta G'^{\ddagger}_{\text{enolate}}$ for propanal reactants (from the data in Fig. 8a) are shown in Table 3.

The formation of condensation and esterification products from a common enolate species (Scheme 4) leads to the rate equations:

$$\frac{r_{\text{aldol}}}{[L]_{\text{TiO2}}} = k_{\text{CC}} K_{\text{al}} P_{\text{propanal}} \theta_{\text{enolate}} \tag{14}$$

$$\frac{r_{\text{ester}}}{[L]_{\text{TiO2}}} = k_{\text{CO}} K_{\text{ol}} K_{\text{H}} P_{\text{propanol}} \theta_{\text{enolate}} \tag{15}$$

Here, k_{CC} and k_{CO} are kinetic constants for the reaction of enolates present at a fractional coverage θ_{enolate} on the active Ti—O site pairs with propanal or 1-propanol to form C—C or C—O bonds, respec-

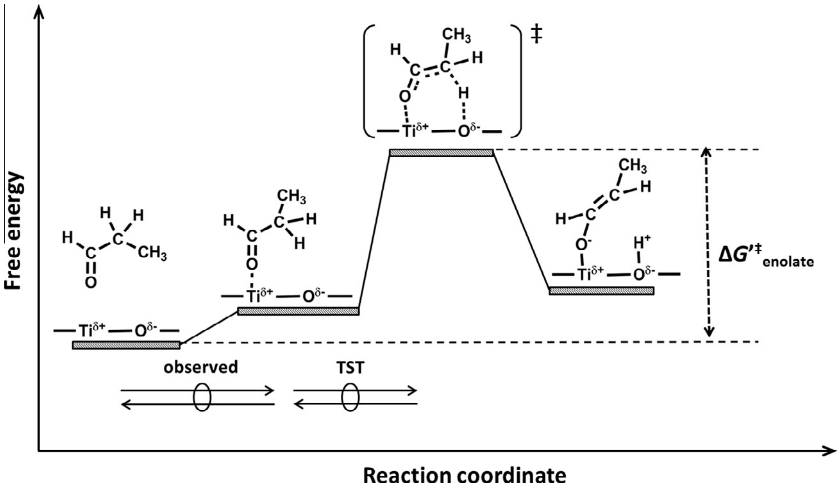

Scheme 5. Schematic reaction coordinate diagram for enolate formation from gaseous propanal on a Ti—O site pair of TiO_2. $\Delta G'^{\ddagger}_{\text{enolate}}$ represents the experimentally accessible apparent free energy barrier of the enolate formation (Eq. (12)).

Table 3
Values of k'_{enolate} and $(k_{CO}K_{ol}K_H)/(k_{CC}K_{al})$ from rate data regressed to the respective functional forms of Eqs. (10) and (16) and the corresponding ΔG values for propanal and acetone reactants.

Reactant	k'_{enolate} (Ti—O ks)$^{-1}$	$\Delta G'^{\ddagger}_{\text{enolate}}$ [c] (kJ mol^{-1})	$(k_{CO}K_{ol}K_H)/(k_{CC}K_{al})$	$\Delta\Delta G^{\ddagger}_{\text{ester-aldol}}$ [d] (kJ mol^{-1})
Propanal[a]	188 ± 5	124 ± 1	0.101 ± 0.03	10 ± 1
Acetone[b]	86.4 ± 0.8	134 ± 1		
Acetone-d_6[b]	35.3 ± 0.2	138 ± 1		

[a] From data in Fig. 8.
[b] From data in Fig. 9.
[c] From Eq. (12).
[d] From Eq. (21).

tively; K_H is equilibrium constant for the H-shift from 1-propanol to enolates on Ti—O site pairs (Step 9, Scheme 4). The esterification/condensation ratios derived from Eqs. (14) and (15) agree with their measured dependence on 1-propanol/propanal ratios (Fig. 8b) and are given by

$$\frac{r_{\text{ester}}}{r_{\text{aldol}}} = \frac{k_{CO}K_{ol}K_H P_{\text{propanol}}}{k_{CC}K_{al}P_{\text{propanal}}} \tag{16}$$

The measured slope in Fig. 8b thus reflects the value of the $(k_{CO}K_{ol}K_H)/(k_{CC}K_{al})$ coefficient in Eq. (16). As in the case of k'_{enolate}, $k_{CO}K_{ol}K_H$ and $k_{CC}K_{al}$ in Eqs. (14) and (15) depend on free energy barriers:

$$k_{CO}K_{ol}K_H = \frac{k_B T}{h}\exp\left(-\frac{\Delta G^{\ddagger}_{\text{ester}}}{RT}\right) \tag{17}$$

$$k_{CC}K_{al} = \frac{k_B T}{h}\exp\left(-\frac{\Delta G^{\ddagger}_{\text{aldol}}}{RT}\right) \tag{18}$$

where $\Delta G^{\ddagger}_{\text{ester}}$ represents the free energy of the C—O coupling transition state ($G^{\ddagger}_{\text{ester}}$) relative to a gaseous 1-propanol (G_{ol}) and an adsorbed enolate on a T—O site pair (G_{enolate}) (Scheme 6):

$$\Delta G^{\ddagger}_{\text{ester}} = G^{\ddagger}_{\text{ester}} - G_{ol} - G_{\text{enolate}} \tag{19}$$

and $\Delta G^{\ddagger}_{\text{aldol}}$ represents the free energy of the C—C coupling transition state ($G^{\ddagger}_{\text{aldol}}$) relative to a gaseous propanal (G_{al}) and the bound enolate (G_{enolate}) (Scheme 6):

$$\Delta G^{\ddagger}_{\text{aldol}} = G^{\ddagger}_{\text{aldol}} - G_{al} - G_{\text{enolate}} \tag{20}$$

Eqs. (17) and (18), taken together, show that the $(k_{CO}K_{ol}K_H)/(k_{CC}K_{al})$ coefficient reflects the free energy barrier difference ($\Delta\Delta G^{\ddagger}_{\text{ester-aldol}}$) between $\Delta G^{\ddagger}_{\text{ester}}$ and $\Delta G^{\ddagger}_{\text{aldol}}$ as given by

$$\frac{k_{CO}K_{ol}K_H}{k_{CC}K_{al}} = \exp\left(-\frac{\Delta\Delta G^{\ddagger}_{\text{ester-aldol}}}{RT}\right) \tag{21}$$

in which

$$\Delta\Delta G^{\ddagger}_{\text{ester-aldol}} = G^{\ddagger}_{\text{ester}} - G^{\ddagger}_{\text{aldol}} + G_{al} - G_{ol} \tag{22}$$

The data in Fig. 8b, used in Eq. (21), give a $\Delta\Delta G^{\ddagger}_{\text{ester-aldol}}$ value of 10 ± 1 kJ mol^{-1} (at 523 K; Table 3) for 1-propanol–propanal reactants, reflecting a modest preference for enolate reactions with propanal over those with 1-propanol on Ti—O site pairs at anatase surfaces.

The mechanistic interpretation of acetone condensation rates is similar to that shown above for propanal reactions, albeit without parallel esterification reaction routes from the enolates formed. The approach to equilibrium between 2-propanol and acetone was also near unity at all conditions (TiO_2(P25) + Cu/SiO_2 (1:1 mass); Fig. 9). Acetone condensation rates were proportional to acetone pressures, insensitive to 2-propanol pressures, and independent of whether acetone pressures were achieved from acetone or 2-propanal as reactants, because of their fast interconversions on the Cu function (Fig. 9).

Scheme 7 depicts acetone condensation pathways similar to those shown above for propanal reactions on TiO_2 surfaces (Scheme 4); the elementary steps include α-H abstraction from acetone to form enolates (Steps 1–2), C—C coupling between enolate and a vicinal bound acetone (Steps 3–4), and dehydration to

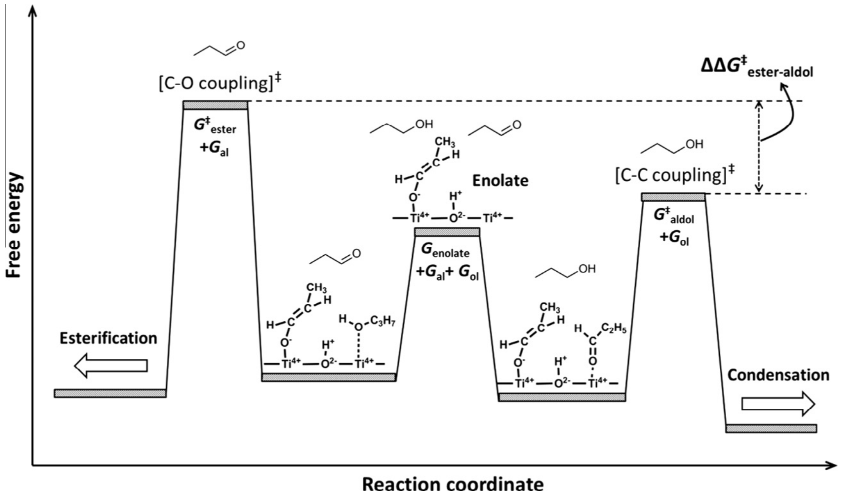

Scheme 6. Schematic reaction coordinate diagram for the formation of C—C and C—O bonds via reactions of propanal-derived enolates with propanal and 1-propanol at Ti—O site pairs on TiO_2 surfaces. [C—O coupling]‡ and [C—C coupling]‡ represent respective transition states for the C—O coupling (Step 10; Scheme 4) and C—C coupling (Step 4; Scheme 4), respectively; $\Delta\Delta G'^{\ddagger}_{ester-aldol}$ values are measurable activation free energy barrier differences between esterification and condensation reactions (Eq. (21)).

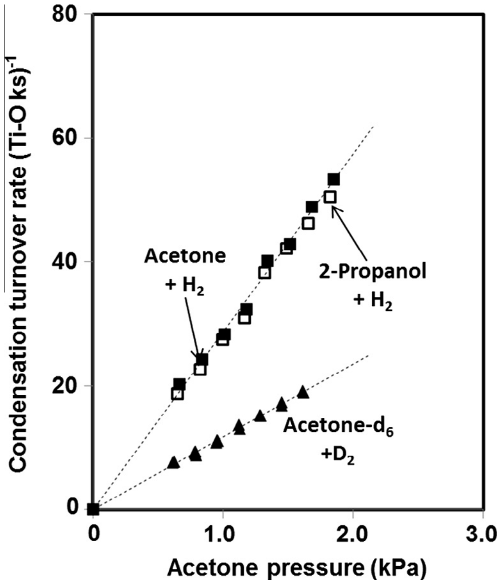

Fig. 9. Acetone pressure effects on aldol condensation turnover rates with 2-propanol (□), acetone (■) and acetone-d_6 (▲) as reactants (TiO_2(P25) + 20 wt.% Cu/SiO_2 (1:1 mass), 523 K, 0.8–2.0 kPa oxygenates, 40 kPa H_2 for 2-propanol and acetone, 40 kPa D_2 for acetone-d_6). Dashed lines represent the regressed fits to the functional form of Eq. (23).

form mesityl oxide (Steps 5–7). As in the case of propanal reactants, the linear relation between rates and acetone pressures indicates that α-H abstraction is the sole kinetically-relevant step; it occurs on Ti—O site pairs essentially uncovered during catalysis, thus leading to the rate equation:

$$\frac{r_{enolate}}{[L]_{TiO2}} = \frac{r_{aldol}}{[L]_{TiO2}} = k_{enolate}K_{one}P_{acetone} = k'_{enolate}P_{acetone} \qquad (23)$$

where $[L]_{TiO2}$ is the number of Ti—O pairs, $r_{enolate}$ and r_{aldol} are the respective enolate formation and aldol condensation rates, $k_{enolate}$ is rate constant for enolate formation from acetone, K_{one} is acetone adsorption constant on exposed anatase Ti—O site pairs, and $k'_{enolate}$ represents the apparent rate constant for condensation ($k_{enolate}K_{one}$). As in Eq. (12) (for propanal reactants), $k'_{enolate}$ reflects the free energy of the enolate formation TS relative to a gaseous acetone molecule and an unoccupied Ti—O site pair ($\Delta G'^{\ddagger}_{enolate}$, defined by Eq. (13)). Measured rate constants (Fig. 9) give a $\Delta G'^{\ddagger}_{enolate}$ value of 134 ± 1 kJ mol^{-1} (523 K, Table 3), which is 10 ± 2 kJ/mol higher than for enolate formation from propanal (124 ± 1 kJ mol^{-1}; 523 K, Table 3). The relative reactivities implied by these different activation free energies are consistent with the higher DFT-derived deprotonation energy (DPE) at the α-C-atom in gaseous acetone (1648 kJ mol^{-1}) than in gaseous propanal (1622 kJ mol^{-1}), as described in Section 3.5.

Condensation rates were also proportional to the alkanone pressure for perdeuterated acetone (acetone-d_6; D_2 used instead of H_2 to avoid isotopic dilution of reactants) (Fig. 9). Acetone-d_6 condensation rates were lower than for undeuterated acetone, with a rate constant ratio $((k'_{enolate})_H/(k'_{enolate})_D)$ of 2.4 (523 K, Table 3); such primary kinetic isotope effects are consistent with the kinetic relevance of α-C—H bond cleavage steps required for enolate formation. This $((k'_{enolate})_H/(k'_{enolate})_D)$ value is nearly identical to that derived from DFT methods (2.5; Section 3.5).

These kinetic effects of alkanal and alkanone pressures show that condensation and esterification rates are limited by the formation of enolates from carbonyl reactants. The subsequent enolate reaction steps, to form C—C or C—O bonds in molecules with the O-contents and backbones expected from nucleophilic attacks, determine the products formed but not their combined formation rates. Next, we assess these mechanistic hypotheses using theoretical treatments, while also examining the reactivity descriptors that determine the effectiveness of Ti—O site pairs for enolate formation and for the selectivity to condensation and esterification products (Section 3.4) and the very different reactivities of anatase and rutile TiO_2 surfaces (Section 3.3).

3.5. Density functional theory treatments of aldol condensation and esterification on $Ti_5O_{19}H_{18}$ cluster models

The condensation pathways in Schemes 4 and 7 involve two Ti Lewis acid centers and one basic O-atom vicinal to these two Ti-atoms. These Ti—O—Ti structures were examined using clusters constructed from the (101) plane of TiO_2(a), the most stable anatase surface [31]; this surface consists of sawtooth-like features with two Ti-atoms and two O-atoms that are distinct in coordination number (CN) as shown in Scheme 1a. One Ti center is under-coordinated (Ti_{5c}, CN 5) and the other exhibits octahedral

(A) Enolate formation form acetone

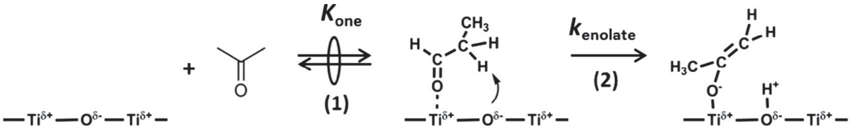

(B) Aldol condensation reaction between enolate and acetone

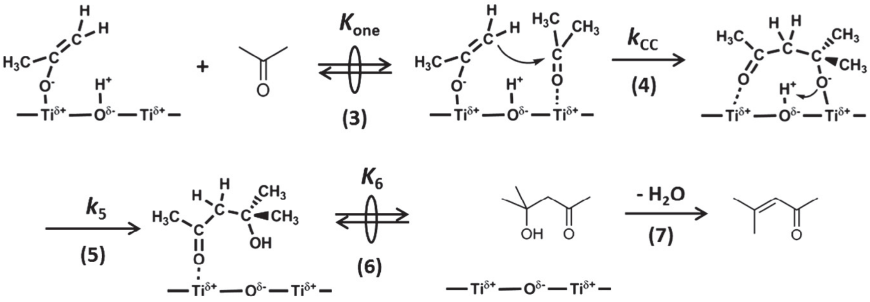

Scheme 7. Aldol condensation pathway of 2-propanol–acetone reactants on bifunctional $TiO_2 + Cu/SiO_2$ catalysts. Reaction numbers used throughout the text are in parentheses (e.g., (1)) below each reaction arrow; k_j and K_j are kinetic constant of the forward step and equilibrium constant for Step j, respectively.

coordination, making it coordinatively saturated (Ti_{6c}, CN 6). Bridging (O_{2c}, CN 2) and in-plane (O_{3c}, CN 3) O-anions link these Ti centers. Here, we use a symmetrical $Ti_5O_{19}H_{18}$ cluster, extracted from anatase (101) surfaces, to describe these structures and their binding and catalytic properties (Scheme 1a), because these properties on oxides, in contrast to metals, predominantly reflect the local properties near the binding sites [34]; the low surface coverages prevalent at the examined catalytic conditions (Section 3.4) exclude significate lateral interactions among adsorbed species, which would require multiple site pairs for accurate treatments. These clusters consist of five Ti-atoms (2 Ti_{5c}, 3 Ti_{6c}) and three O-atoms (1 O_{3c}, 2 O_{2c}) with H-atoms placed at the O-atoms in the cluster edge, in order to terminate the cluster while maintaining charge neutrality (Section 2.4).

The strength of the Lewis acid centers in these clusters was probed using the affinity of each distinct Ti center for gaseous OH^- anions (E_{HA}, Eq. (2)), while basic strength for O-atoms was assessed using their affinity for gaseous protons (E_{PA}, Eq. (3)) (Table 4). The hydroxide anion affinity is $-389\ kJ\ mol^{-1}$ for Ti_{5c} centers and less negative than $-1\ kJ\ mol^{-1}$ for the coordinatively-saturated Ti_{6c} centers (Table 4), indicating that only Ti_{5c} centers could stabilize enolate formation transition states. The proton affinities for O_{2c} and O_{3c} sites are similar (-1009 and $-1008\ kJ\ mol^{-1}$, respectively; Table 4); therefore, their involvement and reactivity depend predominantly on their distance from the active Ti_{5c} centers, because of the concerted interactions required to stabilize transition states along the reaction coordinate for enolate formation and for subsequent reactions of such enolate species (Scheme 4). Each O_{2c} site is linked to one Ti_{5c} site (0.183 nm) and one Ti_{6c} site (0.184 nm), but resides far from a second Ti_{5c} site (0.433 nm), which would be required to bind the second carbonyl or alkanol reactant to complete C—C or C—O formation turnovers; in contrast, each O_{3c} site binds to two acidic Ti_{5c} sites with identical bond lengths (0.203 nm). The involvement of these Ti_{5c}—$O_{2c/3c}$—Ti_{5c} sites in the elementary steps of Scheme 4 is assessed next using DFT methods by calculating enthalpies, entropies, and free energies for these steps.

Table 4
Coordination numbers (CN), hydroxide anion affinities (E_{HA}), and proton affinities (E_{PA}) for exposed atoms on TiO_2(a) (101) surface (Scheme 1a).

Site	CN	E_{HA}[a] ($kJ\ mol^{-1}$)	E_{PA}[a] ($kJ\ mol^{-1}$)
Ti_{5c}	5	−389	
Ti_{6c}	6	<−1	
O_{2c}	2		−1008
O_{3c}	3		−1009

[a] $Ti_5O_{19}H_{18}$ cluster model, B3LYP, 6-311+G(d,p) for C, H, and O-atoms, LANL2DZ for Ti-atoms.

The proposed propanal condensation and esterification elementary steps (Scheme 4) were examined at Ti_{5c}—O_{3c}—Ti_{5c} sites on anatase $Ti_5O_{19}H_{18}$ clusters (Scheme 1a). DFT-derived enolate formation transition states (from propanal; Step 2, Scheme 4) involve α-C—H cleavage (Scheme 8) and concerted interactions with the basic O_{3c} site, which abstracts the α-H atom from propanal (α-H-O_{3c} 0.127 nm), and the acidic Ti_{5c} center, which concurrently interacts with the carbonyl O-atom (Ti_{5c}—O 0.199 nm). The α-C—H bond at the TS is longer than in propanal reactants (0.140 vs. 0.109 nm, Scheme 8), but much shorter than the combined van der Waals radii of C and H-atoms (0.29 nm), indicating that the α-C—H bond is not fully cleaved at the enolate formation TS. As the α-C—H bond cleaves along the reaction coordinate, the C=O bond in propanal weakens and lengthens, as its O-atom interacts with the Ti_{5c} site, leading to C=O bonds that are longer at the TS (0.128 nm) than in propanal reactants (0.122 nm); these bonds ultimately increase to 0.134 nm in the fully-formed enolate product state (Scheme 8).

The evolution of these structures on Ti_{5c}—O_{3c} site pairs indicates that the TS lies at an intermediate point along the α-C—H bond activation path and that it is neither very late nor very early along the reaction coordinate. In addition, the local atomic charges of the structures involved, determined from the natural bond orbital (NBO) theory using bonding orbitals with maximum electron density to determine the most possible Lewis electronic structure [45], indicate that the electron transfer between propanal and the $Ti_5O_{19}H_{18}$ cluster is negligible throughout the enolate formation reaction coordinate (<0.1 e, Table 5); this confirms that Ti_{5c}—O_{3c} site pairs act as Lewis acid–base site pairs without significant redox character.

The condensation and esterification elementary steps after the enolate formation (Scheme 4) were also examined at the same level of theory; DFT-derived structures of the relevant reactants, transition states, and products are shown in the SI (Section S5). These theoretical treatments notably showed that C—O coupling between enolates and alkanols cannot occur in one elementary step, but requires instead sequential steps involving hydrogen shift and C—O bond formation (Steps 9 and 10; Scheme 4).

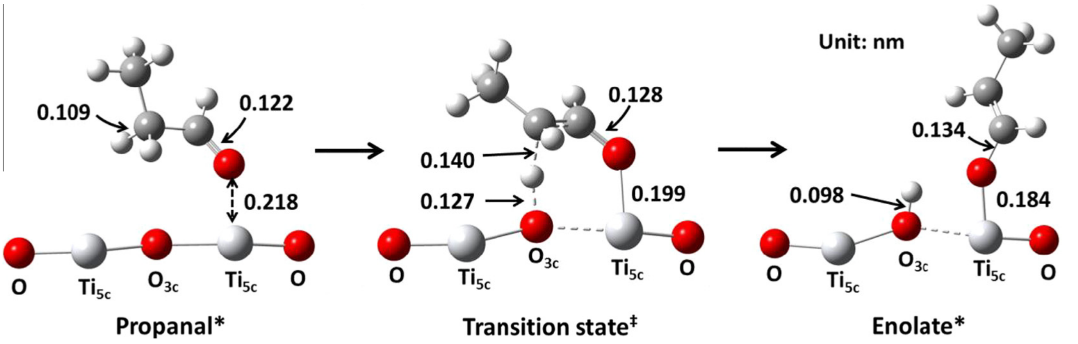

Scheme 8. DFT-derived structures involved in enolate formation reactions from propanal on Ti_{5c}—O_{3c}—Ti_{5c} sites of the anatase $Ti_5O_{19}H_{18}$ cluster (B3LYP, 6-311G(d,p) for C, H, and O-atoms, LANL2DZ for Ti-atoms; only Ti_{5c}—O_{3c}—Ti_{5c} sites and two O-atoms directly bound with the Ti_{5c} sites are shown for clarity).

Table 5
Local charges of optimized structures involved in enolate formation of propanal on Ti_{5c}—O_{3c}—Ti_{5c} sites of the anatase $Ti_5O_{19}H_{18}$ cluster obtained from nature bond orbital analysis.[a]

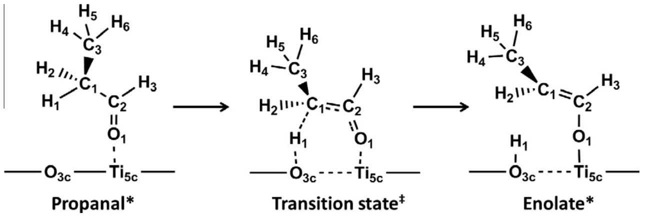

Atom	Propanal*	Transition state‡	Enolate*
C_1	−0.50	−0.53	−0.27
C_2	0.59	0.47	0.17
C_3	−0.57	−0.58	−0.59
O_1	−0.51	−0.60	−0.64
H_1	0.26	0.42	0.55
H_2	0.24	0.26	0.22
H_3	0.13	0.16	0.15
H_4	0.21	0.21	0.20
H_5	0.20	0.20	0.19
H_6	0.19	0.20	0.19
Sum	0.24	0.21	0.17

[a] B3LYP, 6-311G(d,p) for C, H, and O-atoms, LANL2DZ for Ti-atoms.

The free energy reaction coordinate diagrams are depicted in Fig. 10 for aldol condensation and esterification reactions of 1-propanol–propanal reactants on Ti_{5c}—O_{3c}—Ti_{5c} sites of the anatase $Ti_5O_{19}H_{18}$ cluster. All energies are referenced to a bare $Ti_5O_{19}H_{18}$ cluster and the respective gaseous 1-propanol or propanal reactants, and free energies are given at 523 K and 1 bar. The corresponding enthalpy and entropy components are reported in the SI (Section S5). The free energy of the enolate TS from propanal reactants (122 kJ mol^{-1}), corresponding to $\Delta G'^{\ddagger}_{enolate}$ in Eq. (13), is higher than those for the subsequent C—C and C—O formation steps, consistent with the kinetic relevance of a common α-C—H bond cleavage in the formation of esterification and condensation products and in agreement with the experimental measurements (124 ± 1 kJ mol^{-1}, Table 3). The DFT-derived Gibbs free energy for adsorbed propanal at the Ti_{5c} site on the $Ti_5O_{19}H_{18}$ cluster (ΔG_{ads}) is 1 kJ mol^{-1} (Fig. 10), which gives, in term, an equilibrium adsorption constant (K_{al}):

$$K_{al} = \exp\left(\frac{-\Delta G_{ads}}{RT}\right) \tag{24}$$

of 0.008 kPa^{-1}, consistent with surfaces that are essentially uncovered by intermediates during catalysis at the conditions of this study and even at much higher propanal pressures (e.g. 0.07 at 10 kPa) and with the observed rate equation and its mechanistic interpretation (Eq. (10) and Scheme 4).

The TS for the enolate–propanal C—C coupling step (Step 4, Scheme 4) showed the highest free energy along the enolate reaction branch leading to condensation products (76 kJ mol^{-1}, Fig. 10); therefore, this step accounts for the value of $\Delta G^{\ddagger}_{C-C}$ in Eq. (20). The TS for alkoxide–alkanal C—O coupling, which occurs after the H-transfer from 1-propanol to the enolate (Step 10; Scheme 4), showed the highest free energy along the enolate reaction branch that leads to esterification products (89 kJ mol^{-1}, Fig. 10), thus accounting for the value of $\Delta G^{\ddagger}_{C-O}$ in Eq. (19). The value of $\Delta\Delta G^{\ddagger}_{ester-aldol}$ (Eq. (22)) calculated from the free energy difference between $\Delta G^{\ddagger}_{C-C}$ and $\Delta G^{\ddagger}_{C-O}$ is 13 kJ mol^{-1} (Fig. 10), also agreed well with the experimentally-measured value (10 ± 1 kJ mol^{-1}, Table 3).

These propanal condensation pathways (Scheme 4) were also examined at Ti_{5c}—O_{2c}—Ti_{5c} sites on anatase $Ti_5O_{19}H_{18}$ clusters (Scheme 1a); the DFT-derived structures of the reactants, transition states, and products involved (shown in Section S6, SI) are similar to those at Ti_{5c}—O_{3c}—Ti_{5c} sites, but with O_{2c} instead of O_{3c} sites as the α-H-atom abstractor and with the proton bound at the O_{2c} site before reprotonation of the bound product of the enolate–propanal C—C coupling step (Step 5; Scheme 4). The free energies of transition states involved in enolate formation and its C—C coupling reaction (Steps 2 and 4; Scheme 4) were both ~15 kJ mol^{-1} smaller than at Ti_{5c}—O_{3c}—Ti_{5c} sites (referenced to a bare $Ti_5O_{19}H_{18}$ cluster and two gaseous propanal reactants, 523 K and 1 bar; Section S6, SI).

The greater stability of these enolate formation and C—C coupling transition states on the Ti_{5c}—O_{2c}—Ti_{5c} sites reflects shorter Ti_{5c}—O_{2c} bonds (0.183 nm) than in Ti_{5c}—O_{3c}—Ti_{5c} sites (0.203 nm), even though Ti_{5c}—O_{3c}—Ti_{5c} and Ti_{5c}—O_{2c}—Ti_{5c} sites have identical acid and base properties (Table 4). The Ti_{5c}—O_{2c} bonds allow more effective concerted coordination at transition states, as evident from the shorter α-C—H bond at the enolate formation TS for Ti_{5c}—O_{2c} (0.136 nm, Section S6, SI) than for Ti_{5c}—O_{3c} site pairs (0.140 nm, Scheme 8). The reprotonation TS of the aldol precursor (Step 5; Scheme 4), however, was 79 kJ mol^{-1} higher on Ti_{5c}—O_{2c}—Ti_{5c} than on Ti_{5c}—O_{3c}—Ti_{5c} sites ($\Delta G^{\ddagger}_{reprot}$: 129 vs. 50 kJ mol^{-1}; Section S6, SI), as a consequence of the much larger distance between the proton and the aldol precursor on Ti_{5c}—O_{2c}—Ti_{5c} sites (0.396 nm, Section S6, SI), compared to the corresponding distance on Ti_{5c}—O_{3c}—Ti_{5c} sites (0.188 nm, Section S5, SI). On Ti_{5c}—O_{2c}—Ti_{5c} sites, the reprotonation TS had a higher free energy than those involved in enolate formation (108 kJ mol^{-1}) and C—C coupling (58 kJ mol^{-1}) transition states (Section S6, SI), thus making reprotonation the kinetically-relevant step and its overall activation free energy higher than on Ti_{5c}—O_{3c}—Ti_{5c} sites (129 vs. 122 kJ mol^{-1}). The kinetic relevance of

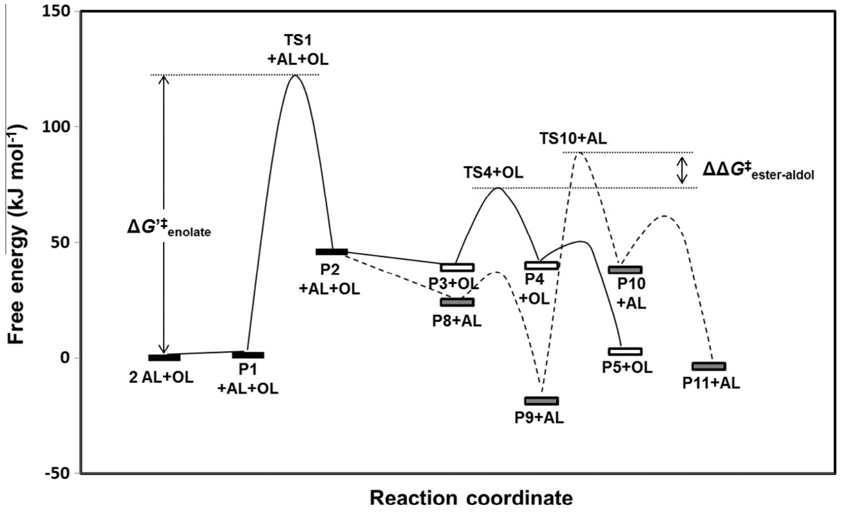

Fig. 10. DFT-derived reaction free energy diagram of aldol condensation (solid lines) and esterification (dashed lines) pathways for 1-propanol–propanal reactants on Ti_{5c}—O_{3c}—Ti_{5c} sites of the anatase $Ti_5O_{19}H_{18}$ cluster (B3LYP, 6-311G(d,p) for C, H, and O-atoms, LANL2DZ for Ti-atoms; 523 K, 1 bar). TSj and Pj represent the respective transition state and product of Step *j* in Scheme 4. Energies are relative to a bare cluster and two gaseous propanal (AL) and one gaseous 1-propanol (OL).

this reprotonation step, taken together with DFT-estimated negligible propanal coverages on Ti_{5c} sites as described above (ΔG_{ads} 1 kJ mol^{-1}, Fig. 10), leads to a rate equation:

$$\frac{r_{aldol}}{[L]_{TiO2}} = \frac{k_B T}{h} e^{-\frac{\Delta G^{\ddagger}_{reprot}}{RT}} (P_{propanal})^2 \tag{25}$$

for aldol condensation rates (r_{aldol}) on Ti_{5c}—O_{2c}—Ti_{5c} sites (derivation details in Section S6, SI), which is inconsistent with the measured first-order rate dependence on propanal pressure (Section 3.4). Moreover, the overall activation free energy difference for propanal condensation on Ti_{5c}—O_{2c}—Ti_{5c} (129 kJ mol^{-1}) and Ti_{5c}—O_{3c}—Ti_{5c} (122 kJ mol^{-1}) sites leads to a ratio of 0.0004 for condensation rates on Ti_{5c}—O_{2c}—Ti_{5c} sites to those on Ti_{5c}—O_{3c}—Ti_{5c} sites at 523 K and 0.18 kPa propanal (a typical condition examined in this study), according to Eqs. (11) and (25); the much lower reactivity of Ti_{5c}—O_{2c}—Ti_{5c} sites compared to Ti_{5c}—O_{3c}—Ti_{5c} sites reflects that modest distances of the O site with the two Ti sites involved in the Ti—O—Ti sites are required for efficient aldol condensation turnovers. This spatial consequence of Ti—O—Ti sites was also found on TiO_2(r) (110) surfaces, which renders TiO_2(r) (110) surfaces inactive for aldol condensation turnovers (Section S8, SI).

Ti_{5c}—O_{3c}—Ti_{5c} sites were chosen to examine acetone condensation pathways (Scheme 7) using DFT methods. DFT-derived TS structures for enolate formation are similar for acetone (Scheme 9) and propanal (Scheme 8); in both cases, TS structures involve concerted interactions of Ti_{5c} and O_{3c} sites with carbonyl O-atoms and α-H-atoms in the enolate precursors, respectively. Acetone-derived TS structures exhibited a slightly longer α-C—H bond than for propanal (0.143 vs. 0.140 nm, Schemes 8 and 9) and a slightly shorter α-H-O_{3c} bond (0.123 vs. 0.127 nm, Schemes 8 and 9), consistent with a TS that occurs somewhat later along the reaction coordinate and with the different deprotonation energies (E_{DPE}) of their respective α-C—H bonds. These energies are given by

$$E_{DPE} = E_{Z^-} + E_{H^+} - E_{HZ} \tag{26}$$

where E_{HZ}, E_Z^-, and E_H^+ are respective electronic energies of a neutral molecule (HZ), the anion deprotonated from HZ (Z^-), and a bare gaseous proton. DFT-derived DPE values for the α-H-atoms in propanal and acetone were 1622 and 1648 kJ mol^{-1}, respectively (Table 6), consistent with the latter TS for the bond with the larger heterolytic dissociation energy. DFT-derived structures of the reactants, transition states, and products are similar for enolate formation and C—C coupling steps in acetone and propanal reactions (Section S7, SI), indicative of the general nature of these condensation pathways on acid–base site pairs.

Fig. 11 depicts the free energy reaction coordinate diagram for acetone condensation (Scheme 7; the respective enthalpies and entropies are shown in Section S7, SI), referenced to a bare $Ti_5O_{19}H_{18}$ cluster and two gaseous acetone molecules. The enolate formation TS gives the highest free energy along the reaction coordinate (Fig. 11), indicating that this is the sole kinetically-relevant step, as found for propanal, consistent with the measured first-order condensation rate dependence on acetone pressure (Fig. 9) and the normal kinetic H/D isotope effect (2.4, 523 K, Table 3). The free energy of the enolate formation TS thus accounts for the

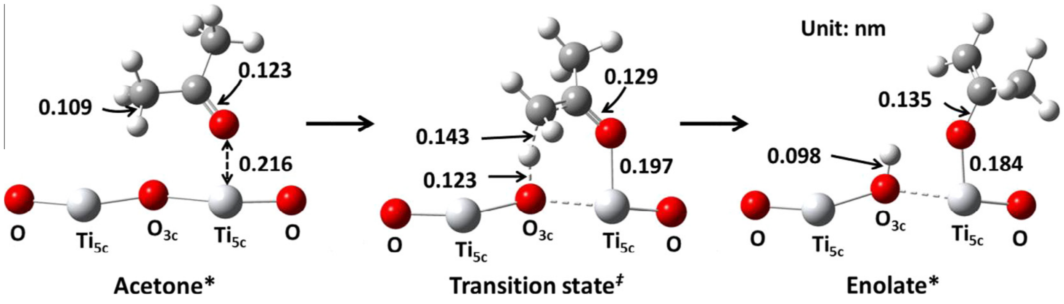

Scheme 9. DFT-derived structures involved in enolate formation reactions from acetone on Ti_{5c}—O_{3c}—Ti_{5c} sites of the anatase $Ti_5O_{19}H_{18}$ cluster (B3LYP, 6-311G(d,p) for C, H, and O-atoms, LANL2DZ for Ti-atoms; only Ti_{5c}—O_{3c}—Ti_{5c} sites and two O-atoms directly bound with the Ti_{5c} sites are shown for clarity).

Table 6
Deprotonation energy (E_{DPE}) of α-H-atom and DFT-derived $\Delta H'^{\ddagger}_{enolate}$, $\Delta S'^{\ddagger}_{enolate}$ and $\Delta G'^{\ddagger}_{enolate}$ for propanal, acetone, and acetone-d_6 reactants.[a]

Reactant	E_{DPE} (kJ mol^{-1})	$\Delta H^{\ddagger}_{enolate}$ (kJ mol^{-1})	$\Delta S^{\ddagger}_{enolate}$ (J mol^{-1} K^{-1})	$\Delta G^{\ddagger}_{enolate}$ (kJ mol^{-1})
Propanal	1622	9	−215	122
Acetone	1648	17	−217	131
Acetone-d_6	1648	21	−217	135

[a] Using Ti_{5c}—O_{3c}—Ti_{5c} sites of the anatase $Ti_5O_{19}H_{18}$ cluster; 523 K, 1 bar, B3LYP, 6-311G(d,p) for C, H, and O-atoms, and LANL2DZ for Ti-atoms.

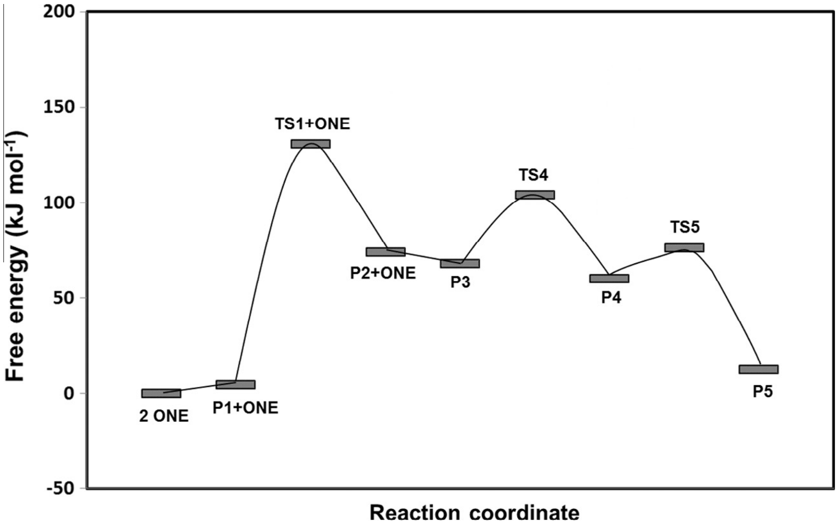

Fig. 11. DFT-derived reaction free energy diagram of acetone condensation on Ti_{5c}—O_{3c}—Ti_{5c} sites of the anatase $Ti_5O_{19}H_{18}$ cluster (B3LYP, 6-311G(d,p) for C, H, and O-atoms, LANL2DZ for Ti-atoms; 523 K, 1 bar). TSj and Pj represent the respective transition state and product of Step *j* in Scheme 7. Energies are relative to a bare cluster and two gaseous acetone reactants (ONE).

measured $\Delta G'^{\ddagger}_{enolate}$ value (Eq. (12); 134 ± 1 kJ mol^{-1}, Table 3), which agrees well with the theoretical estimate (131 kJ mol^{-1}, Table 6). The DFT-derived $\Delta G'^{\ddagger}_{enolate}$ value for acetone-d_6 reactants was 4 kJ mol^{-1} larger than for undeuterated acetone (Table 6), as a result of the larger free energy difference between the enolate formation TS and the gaseous reactant for deuterated species; this free energy difference gives a kinetic isotope effect of 2.5 $((k'_{enolate})_H/(k'_{enolate})_D)$ at 523 K, consistent with the measured value (2.4, Table 3).

DFT-derived enthalpy $(\Delta H'^{\ddagger}_{enolate})$ and entropy $\left(\Delta S'^{\ddagger}_{enolate}\right)$ contributions to activation free energies $(\Delta G'^{\ddagger}_{enolate})$ are shown in Table 6 for propanal and acetone reactants. $\Delta H'^{\ddagger}_{enolate}$ values were 8 kJ mol^{-1} smaller for propanal than acetone, thus accounting for the reactivity differences between these two molecules ($\Delta G'^{\ddagger}_{enolate}$ difference 9 kJ mol^{-1}). The relative reactivity of these C_3 molecules in enolate formation is thus enthalpy-determined, reflecting their similar entropy changes from a gaseous reactant to the enolate formation TS. $\Delta H'^{\ddagger}_{enolate}$ values depend on DPE (α-H) in reactants because their α-C—H bonds are partially cleaved at the enolate formation TS (Schemes 8 and 9). DPE predominantly depends, in turn, on the effects of substituents on the stability of the anion formed. The methyl group bound at the α-C-atom in propanal leads to more stable enolate species (via p–π conjugation with the C=C bond) than the methyl group at the carbonyl C-atom in acetone, which destabilizes the enolate (via repulsion between the electron-donating methyl group and the O anion in the enolate formed) [54].

Aldol condensation pathways were also examined on TiO_2(r) using the above DFT methods and a $Ti_5O_{19}H_{18}$ cluster extracted from the most stable exposed rutile (1 1 0) plane [31]; detailed results are included in SI (Section S8). These DFT treatments show that relevant Ti—O—Ti sites on rutile (1 1 0) surface have stronger acid and basic characters than the active Ti_{5c}—O_{3c}—Ti_{5c} species on anatase (1 0 1) surface and a longer Ti—O distance on rutile than anatase (0.323 vs. 0.203 nm); these properties lead to the intermediates and transition states involved in acetone condensation on rutile were more stable than on anatase by >50 kJ mol^{-1}. In particular, the dimer species formed in C—C coupling steps (Step 4; Scheme 7) are very strongly-bound (−266 kJ mol^{-1}, referenced to a bare $Ti_5O_{19}H_{18}$ cluster and two gaseous acetone molecules; Section S8, SI), and the difficult reprotonation of these stable dimer species limits the C—C coupling turnovers, which would lead to undetectable rates on rutile (e.g. ~10^{13}-fold lower than on anatase; 523 K, 0.8 kPa acetone). Such difficult reprotonation of the aldol precursors on the relevant Ti—O—Ti sites of rutile reflects the strong acid and basic characters of the Ti and the O sites, respectively, which stabilizes both reactants involved (the precursor at Ti centers and the proton at O sites), combined with their large separation (0.403 nm; Section S8, SI) that is reminiscent of the spatial effects at the less active Ti_{5c}—O_{2c}—Ti_{5c} sites on anatase. The free energy barrier from the bound dimer species to the reprotonation TS was much larger on rutile (289 kJ mol^{-1}, 523 K; Section S8, SI) than at Ti_{5c}—O_{2c}—Ti_{5c} sites on anatase (116 kJ mol^{-1}, 523 K; Section S7, SI), in spite of their similar distances between the aldol precursor and the proton (0.403 vs. 0.396 nm), indicating that acid–base strength, instead of the distance between the aldol precursor and the proton, accounts for the difficult reprotonation, and thus the unreactive nature of TiO_2(r) surfaces.

In summary, we conclude that aldol condensation turnovers require acid–base site pairs of moderate acid–base strength, located within moderate distances to allow the concerted stabilization of enolate formation transition states while preventing the standing of condensation products by the strong stabilization of aldol precursors and protons by pairs with strong acid and basic sites, respectively. These conclusions apply also to reactions of C_2–C_5 alkanals and alkanones and for acid–base site pairs on other oxides (monoclinic and tetragonal ZrO_2) [29]. Notably, the site pairs of moderate acid–base strength required for condensation and esterification turnovers also prevent the strong inhibition by H_2O (or CO_2) ubiquitous on strongly basic oxides [55], leading to high turnover rates even at high conversions. When protected through these bifunctional strategies conferred by H_2, TiO_2(a) and ZrO_2 allow high and stable condensation and esterification rates and selectivities at practical conditions.

4. Conclusions

Addition of a Cu cocatalyst and H_2 removes thermodynamic constraints and avoids deactivation for TiO_2-catalyzed propanal and acetone condensation reactions by scavenging equilibrium-limited unsaturated condensation products to more stable alkanals, alkanones, and alkanols; the hydrogenation–dehydrogenation function conferred by Cu also equilibrates C_3 alkanols and their carbonyl analogs, providing lumped reactant pools, and catalyzes esterification for 1-propanol–propanal reactants. This bifunctional strategy increases net rates, selectivity and stability of TiO_2-catalyzed aldol condensation reactions over a large range of conversions, rendering these reactions practical for chain growth and O-removal of oxygenates.

Ti—O site pairs of intermediate acid–base strength and Ti—O distances, prevalent on anatase surfaces (but not rutile surfaces), principally account for measured condensation and esterification rates on TiO_2; these active Ti—O site pairs were counted accurately via site titration with propanoic acid during catalysis, allowing for rigorous calculations of turnover rates and activation free energy barriers. Enolate formation from alkanal (alkanone) reactants on sparsely covered Ti—O site pairs, using basic O sites to abstract α-H-atoms and acidic Ti sites to stabilize enolate moieties concertedly, is kinetically-relevant to both aldol condensation and esterification turnover rates; the dependence of enolate formation turnover rates on alkanal (alkanone) reactant pressures reflects the free energy of the enolate formation transition state with respect to a gaseous alkanal (alkanone) reactant and a bare Ti—O site pair. Formed enolate species react via nucleophilic attack either with an alkanal (alkanone) bound on a vicinal Ti site to form an α,β-unsaturated carbonyl compound or with an alkanol bound on the vicinal Ti site to form an hemiacetal intermediate (via sequential H-shift and C—O coupling reactions) followed by dehydrogenation to esters on Cu; esterification/condensation selectivities on Ti—O site pairs are determined by the differences in free energies between enolate-alkanal (C—C) and enolate-alkanol (C—O) coupling transition states and between gaseous alkanal and alkanol reactants.

These mechanistic conclusions are consistent with DFT simulations using anatase cluster models on kinetic consequences of the proposed condensation and esterification elementary steps, and on both isotope and substituent effects on enolate formation rates. Similar simulations on rutile cluster models show that available Ti—O site pairs on rutile surfaces are spatially-separated and have stronger acid–base strength than those on anatase surfaces; aldol condensation reactions on these site pairs are unfeasible because of high free energy barriers required for reprotonation of the C—C coupling products to form aldols. This marked reactivity difference between anatase and rutile surfaces evident from both experiments and theory reveals that Lewis acid–base site pairs of modest acid–base strength and acid–base site distances are preferred for aldol condensation turnovers.

Acknowledgments

The authors acknowledge with thanks thoughtful technical discussions with Drs. Eric Doskocil, John Shabaker, Glenn Sunley, and the rest of the XC^2 program members at BP p.l.c., and with Drs. Stanley Herrmann, Prashant Deshlahra, and Elif Gurbuz at UC-Berkeley throughout the course of this study. The authors are also grateful for the access to computational facilities provided by the Extreme Science and Engineering Discovery Environment (XSEDE) (NSF, grant number ACI-1053575) and the Molecular Graphics and the Computation Facility at the University of California, Berkeley (NSF, grant number CHE-0840505). S.W. kindly acknowledges Dr. Stephanie Kwon (UC-Berkeley) for a careful review of the supporting information. This research project was supported as part of the BP Conversion Consortium (BP-XC^2) at the University of California, Berkeley.

Appendix A. Supplementary material

Supplementary data associated with this article can be found, in the online version, at http://dx.doi.org/10.1016/j.jcat.2016.05.026.

References

[1] G.W. Huber, S. Iborra, A. Corma, Chem. Rev. 106 (2006) 4044–4098.
[2] D.A. Simonetti, J.A. Dumesic, Catal. Rev. 51 (2009) 441–484.
[3] J.C. Serrano-Ruiz, R.M. West, J.A. Dumesic, Annu. Rev. Chem. Biomol. Eng. 1 (2010) 79–100.
[4] T.V. Choudhary, C.B. Phillips, Appl. Catal. A 397 (2011) 1–12.
[5] M.J.A. Tijmensen, A.P.C. Faaij, C.N. Hamelinck, M.R.M. van Hardeveld, Biomass Bioenergy 23 (2002) 129–152.
[6] J. Sun, R.A.L. Baylon, C. Liu, D. Mei, K.J. Martin, P. Venkitasubramanian, Y. Wang, J. Am. Chem. Soc. 138 (2016) 507–517.
[7] N. Li, G.W. Huber, J. Catal. 270 (2010) 48–59.
[8] S. Wang, Y. Zhang, H. Liu, Chem. Asian J. 5 (2010) 1100–1111.
[9] Y. Lin, S. Tanaka, Appl. Microbiol. Biotechnol. 69 (2006) 627–642.
[10] D.A. Simonetti, J.A. Dumesic, ChemSusChem 1 (2008) 725–733.
[11] E.L. Kunkes, D.A. Simonetti, R.M. West, J.C. Serrano-Ruiz, C.A. Gartner, J.A. Dumesic, Science 322 (2008) 417–421.
[12] J.I. Di Cosimo, V.K. Díez, C.R. Apesteguía, Appl. Catal. A 137 (1996) 149–166.
[13] W. Shen, G.A. Tompsett, R. Xing, W.C. Conner Jr., G.W. Huber, J. Catal. 286 (2012) 248–259.
[14] J.I. Di Cosimo, C.R. Apesteguía, M.J.L. Ginés, E. Iglesia, J. Catal. 190 (2000) 261–275.
[15] J.I. Di Cosimo, G. Torres, C.R. Apesteguía, J. Catal. 208 (2002) 114–123.
[16] G. Torres, C.R. Apesteguía, J.I. Di Cosimo, Appl. Catal. A 317 (2007) 161–170.
[17] A.A. Nikolopoulos, B.W.-L. Jang, J.J. Spivey, Appl. Catal. A 296 (2005) 128–136.
[18] M.I. Zaki, M.A. Hasan, L. Pasupulety, Langmuir 17 (2001) 768–774.
[19] E.L. Kunkes, E.I. Gürbüz, J.A. Dumesic, J. Catal. 266 (2009) 236–249.
[20] A. Gangadharan, M. Shen, T. Sooknoi, D.E. Resasco, R.G. Mallinson, Appl. Catal. A 385 (2010) 80–91.
[21] D.G. Hanna, S. Shylesh, Y. Li, S. Krishna, M. Head-Gordon, A.T. Bell, ACS Catal. 4 (2014) 2908–2916.
[22] J.E. Rekoske, M.A. Barteau, Ind. Eng. Chem. Res. 50 (2011) 41–51.
[23] S. Luo, J.L. Falconer, J. Catal. 185 (1999) 393–407.
[24] A.C.C. Rodrigues, J.L.F. Monteiro, Appl. Catal. A 362 (2009) 185–192.
[25] M.J.L. Ginés, E. Iglesia, J. Catal. 176 (1998) 155–172.
[26] E. Iglesia, D.G. Barton, J.A. Biscardi, M.J.L. Gines, S.L. Soled, Catal. Today 38 (1997) 339–360.
[27] M. Singh, N. Zhou, D.K. Paul, K.J. Klabunde, J. Catal. 260 (2008) 371–379.
[28] W. An, Phys. Chem. Chem. Phys. 17 (2015) 22529–22532.
[29] S. Wang, E. Iglesia, Unpublished Work.
[30] C.J.G. van der Grift, P.A. Elberse, A. Mulder, J.W. Geus, Appl. Catal. A 59 (1990) 275–289.
[31] U. Diebold, Surf. Sci. Rep. 48 (2003) 53–229.
[32] W-F. Huang, Hs-T. Chen, M.C. Lin, J. Phys. Chem. C 113 (2009) 20411–20420.
[33] A.V. Bandura, D.G. Sykes, V. Shapovalov, T.N. Troung, J.D. Kubicki, R.A. Evarestov, J. Phys. Chem. B 108 (2004) 7844–7853.
[34] R. Erdogan, M.F. Fellah, I. Onal, Int. J. Quant. Chem. 111 (2011) 174–181.
[35] (a) A.D. Becke, J. Chem. Phys. 98 (1993) 5648–5652;
(b) C. Lee, W. Yang, R.G. Parr, Phys. Rev. B 37 (1988) 785–789.
[36] M.J. Frisch, G.W. Trucks, H.B. Schlegel, G.E. Scuseria, M.A. Robb, J.R. Cheeseman, G. Scalmani, V. Barone, B. Mennucci, G.A. Petersson, H. Nakatsuji, M. Caricato, X. Li, H. P. Hratchian, A.F. Izmaylov, J. Bloino, G. Zheng, J.L. Sonnenberg, M. Hada, M. Ehara, K. Toyota, R. Fukuda, J. Hasegawa, M. Ishida, T. Nakajima, Y. Honda, O. Kitao, H. Nakai, T. Vreven, J. Montgomery, Jr., J.E. Peralta, F. Ogliaro, M. Bearpark, J.J. Heyd, E. Brothers, K.N. Kudin, V.N. Staroverov, R. Kobayashi, J. Normand, K. Raghavachari, A. Rendell, J.C. Burant, S.S. Iyengar, J. Tomasi, M.

Cossi, N. Rega, N.J. Millam, M. Klene, J.E. Knox, J.B. Cross, V. Bakken, C. Adamo, J. Jaramillo, R. Gomperts, R.E. Stratmann, O. Yazyev, A.J. Austin, R. Cammi, C. Pomelli, J.W. Ochterski, R.L. Martin, K. Morokuma, V.G. Zakrzewski, G.A. Voth, P. Salvador, J.J. Dannenberg, S. Dapprich, A.D. Daniels, Ö. Farkas, J.B. Foresman, J. V. Ortiz, J. Cioslowski, D.J. Fox, Gaussian Inc, Wallingford CT, 2009.

[37] (a) A.D. McLean, G.S. Chandler, J. Chem. Phys. 72 (1980) 5639–5648;
(b) R. Krishnan, J.S. Binkley, R. Seeger, J.A. Pople, J. Chem. Phys. 72 (1980) 650–654.

[38] P.J. Hay, W.R. Wadt, J. Chem. Phys. 82 (1985) 270–283.

[39] X. Li, M.J. Frisch, J. Chem. Theor. Comput. 2 (2006) 835–839.

[40] S. Grimme, S. Ehrlich, L. Goerigk, J. Comput. Chem. 32 (2011) 1456–1465.

[41] (a) S.F. Boys, F. Bernardi, Mol. Phys. 19 (1970) 553–566;
(b) S. Simon, M. Duran, J.J. Dannenberg, J. Chem. Phys. 105 (1996) 11024–11031.

[42] J.P. Merrick, D. Moran, L. Radom, J. Phys. Chem. A 111 (2007) 11683–11700.

[43] D.A. McQuarrie, Statistical Mechanics, University Science Books, Sausalito, CA, 2000.

[44] S. Grimme, Chem. Eur. J. 18 (2012) 9955–9964.

[45] R.L. Martin, J. Chem. Phys. 118 (2003) 4775–4777.

[46] T. Clark, J. Chandrasekhar, G.W. Spitznagel, P.v.R. Schleyer, J. Comput. Chem. 4 (1983) 294–301.

[47] L. Mino, G. Spoto, S. Bordiga, A. Zecchina, J. Phys. Chem. C 116 (2012) 17008–17018.

[48] T. Ohno, K. Sarukawa, K. Tokieda, M. Matsumura, J. Catal. 203 (2001) 82–86.

[49] J. Zhang, M. Li, Z. Feng, J. Chen, C. Li, J. Phys. Chem. B 110 (2006) 927–935.

[50] M.E. Sad, M. Neurock, E. Iglesia, J. Am. Chem. Soc. 133 (2011) 20384–20398.

[51] K. Inui, T. Kurabayashi, S. Sato, J. Catal. 212 (2002) 207–217.

[52] E.I. Gürbüz, D.D. Hibbitts, E. Iglesia, J. Am. Chem. Soc. 137 (2015) 11984–11995.

[53] H. Liu, N. Bayat, E. Iglesia, Angew. Chem. Int. Ed. 42 (2003) 5072–5075.

[54] Y. Chiang, M. Hojatti, J.R. Keeffe, A.J. Kresge, N.P. Schepp, J. Wirzt, J. Am. Chem. Soc. 109 (1987) 4000–4009.

[55] H. Hattori, Appl. Catal. A 504 (2015) 103–109.